Journal of Wind Engineering & Industrial Aerodynamics 240 (2023) 105497

Contents lists available at ScienceDirect

Journal of Wind Engineering & Industrial Aerodynamics

journal homepage: www.elsevier.com/locate/jweia

Nested computational fluid dynamic modeling of mean turbulent quantities estimation in complex topography using AROME-SIMRA

Zakari Midjiyawa [a,b,*], Jon Vegard Venås [c], Trond Kvamsdal [b], Arne Morten Kvarving [c], Knut Helge Midtbø [a], Adil Rasheed [c]

[a] Norwegian Meteorological Institute, Henrik Mohns Plass 1, 0313 Oslo, Norway
[b] Department of Mathematical Sciences, Norwegian University of Science and Technology, Alfred Getz' vei 1, 7491 Trondheim, Norway
[c] Department of Mathematics and Cybernetics, SINTEF Digital, Klæbuveien 153, 7465 Trondheim, Norway

ARTICLE INFO

Keywords:
Finite element
Turbulence
Complex terrain
AROME
SIMRA

ABSTRACT

This paper presents a validation of the AROME-SIMRA model, which is a nested computational fluid dynamics model that simulates both mesoscale and microscale phenomena. To validate the model, we analyzed 47 h of mean flow data collected by 13 three-dimensional sonic anemometers. These anemometers were mounted on tall masts located near the shoreline of Sulafjord, with heights ranging from 12 m to 95 m above the ground. Due to the difficulty measuring wind along the bridge span, analyzing flow conditions for the construction of a bridge that spans a vast fjord is a difficult process. Therefore, the primary objective of this study is to validate a nested macroscale–microscale model. This model will be utilized to analyze flow conditions across the span of the proposed bridge crossing in Sulafjord. The study explores the deviation between the measured and the simulated mean turbulence flow characteristics. Only records with the mean wind of 12 m s^{-1} and above at SulaNW met-mast are considered due to their relevance in buffeting response, which led to the identification of a limited number of sectors representative of strong wind conditions. Mean wind speed comparisons show a minimum correlation of 0.6 and a maximum of 0.9 for all the anemometers analyzed. For wind directions, a low correlation between observation and numerical simulation is obtained at SulaSW met-mast located southwest of Sulafjord. A high Angle of Attack is obtained for both simulation and measurements. However, the correlation is dependent on the mast location, wind direction, and anemometer height. Along the bridge span, the flow is largely horizontal for the northwestern flow.

1. Introduction

The Norwegian coastline is renowned for its majestic fjords. However, currently, there is a need for many ferry crossings to accommodate the significant traffic of private and commercial vehicles. Since 2013 the Norwegian Public Roads Administration (NPRA) has been looking at how to replace ferries with bridges to improve transportation time. Evaluation of bridge design requires a rigorous analysis of vortex-induced vibration, buffeting response, and flutter analysis of the bridge, as discussed in previous studies (Simiu and Scanlan, 1996; Scanlan, 1978b,a; Wu and Kareem, 2012). One of the inputs to such analysis is a site-specific characterization of turbulence and wind shear along the span of the bridge. To this end, in 2014, the NPRA launched a large-scale measurement campaign in the fjords of interest for characterizing turbulence conditions. The measurement campaign includes the installation of a met-mast, lidar, and buoy at the fjord's shore, middle, and water surface, respectively, as detailed in Furevik et al. (2019) and Furevik et al. (2020). One of the limitations of any such measurement campaign is the very coarse spatial resolution, which is not appropriate for flow characterization in complex terrain with considerable spatiotemporal variability. Furthermore, it is evident from the campaign that flow characteristics recorded on the shores are not representative of what happens in the middle of the fjord (Midjiyawa et al., 2021). Additionally, the use of point measurement, such as a met-mast, is also influenced by various factors such as surface characteristics, upstream fetch, and location-specific properties.

To address the aforementioned shortcomings of the measured flow parameters (e.g., lack of measurements across the strait), supplementary tools such as computational fluid dynamics (CFD) simulations appear to be a cost- and time-effective alternative. While previous studies have conducted flow simulations around idealized 2D (Cao et al., 2012) or 3D hills (Ding and Street, 2003; Utnes, 2007; Castagna

* Corresponding author at: Norwegian Meteorological Institute, Henrik Mohns Plass 1, 0313 Oslo, Norway.
E-mail address: midjiyawaz@met.no (Z. Midjiyawa).

https://doi.org/10.1016/j.jweia.2023.105497
Received 4 November 2022; Received in revised form 29 June 2023; Accepted 29 June 2023
Available online 13 July 2023

et al., 2012) or terrain validated against wind tunnel data, more realistic simulations involve Large-Eddy Simulations (LES) (Maronga et al., 2015) or hybrid RANS-LES (Bechmann, 2006; Bechmann and Sørensen, 2010, 2011) with realistic terrain. One downside of these models, despite their high accuracy, is their prohibitively high computational cost. URANS (Unsteady Reynolds' Average Navier Stokes), a turbulence modeling approach based on the Boussinesq assumption (Boussinesq, 1877; Schmitt, 2007), provides a trade-off between computational efficiency and accuracy in the modeling of flow conditions in complex topography. These models have been used to analyze turbulence characteristics in sites characterized by irregular terrain using idealized boundary conditions in an offline setting. However, when employing the inlet boundary condition this way, as defined by Richards and Hoxey (1993), without the application of, for example, constant shear stress at the top boundary to incorporate the effect of geostrophic flow, these models are associated with issues related to flow inhomogeneity (Hargreaves and Wright, 2007; Blocken et al., 2007). To this end, wind resource assessment is mostly conducted using offline nested multiscale models covering different ranges of spatio-temporal scales of atmospheric flows. However, the utilization of such coupling in complex topography has not gained widespread application and is linked with significant difficulties associated with its validation in complex terrain (Cheynet et al., 2020). Moreover, most studies in the context of complex terrain rarely present a sound approach to the optimal choice of grid resolution.

In light of the severe shortcomings of the previous studies and the current state-of-the-art, we attempt to address the following issues:

- *Multiscale coupling:* We evaluate the potential of AROME-SIMRA, a meso-micro coupled system with high spatial resolution, in the context of bridge design. AROME, which stands for Application of Research to Operations at the Mesoscale, is a mesoscale numerical weather prediction tool developed by Météo-France (Seity et al., 2011; Müller et al., 2017). SIMRA, which stands for Semi Implicit Reynolds Averaged, is a microscale computational fluid dynamic model developed by SINTEF (Utnes and Eidsvik, 1996; Eidsvik, 2005; Utnes, 2007; Rasheed et al., 2012; Rasheed and Sørli, 2014). The nested AROME-SIMRA is unique in that it balances computational cost-effectiveness and accuracy, and can estimate mean turbulent quantities based on AROME hindcast, nowcast, or forecast data.
- *Model validation:* We validate the coupled system using mean parameters relevant to bridge design, such as wind speed, mean wind direction, and mean angle of attack (AoA). We assess the AROME-SIMRA coupled system using met-mast and lidar measurements taken in Sulafjorden, a fjord on Norway's west coast. A unique aspect of this validation is the quality and quantity of data collected from the measurement campaign.
- *High resolution mesh optimization:* We investigate if a-posteriori error indicators based on continuous global L^2-projection (CGL2) of the error in velocity gradients and pressure can be useful in optimizing the mesh quality. It is worth noting that optimizing high-resolution meshes for use in a multiscale online setting involving complex terrain is not a trivial task but is crucial for running the flow simulation in the atmospheric boundary layer for long durations without divergence.

In Section 2 we present a comprehensive description of the SIMRA, AROME models, and their coupling. It starts with the presentation of the governing equations of SIMRA followed by the details of the numerical discretization which are generally difficult to find. AROME and the nested set-up are presented next followed by the finite element error indicators to be used for mesh optimization. Section 3 presents the placement of the met-mast in Sulafjorden as well as the different processing performed on the data prior to the analysis. Together Sections 2 and 3 should provide all the information required to reproduce the results presented in the article. Results and discussion are presented in Section 5 with a focus on explaining the inconsistencies between measurement and numerical modeling. Finally, the main conclusions from the study are presented in Section 6

2. Governing equations and numerical models

2.1. Governing equations in SIMRA

The detailed formulation of the governing equation along with the different assumptions used in the modeling of stratified flow in complex topography is given in Utnes (2007) and Tabib et al. (2020) and summarized herein for the sake of completeness. Using the Reynolds decomposition $\boldsymbol{u}_{\text{tot}} = \boldsymbol{u} + \boldsymbol{u}'$ where $\boldsymbol{u}$ represents a velocity component in a 3D Cartesian coordinate system, the Reynolds average continuity, momentum, and energy equations in the incompressible form are given by

$$\nabla \cdot (\rho_{\text{s}} \boldsymbol{u}) = 0 \tag{1}$$

$$\frac{\partial \boldsymbol{u}}{\partial t} = -\nabla \left(\frac{p_{\text{d}}}{\rho_{\text{s}}} \right) + \boldsymbol{g} \frac{\theta_{\text{d}}}{\theta_{\text{s}}} + \frac{1}{\rho_{\text{s}}} \nabla \cdot \boldsymbol{\tau} + \boldsymbol{f}, \qquad \boldsymbol{g} = -g \mathbf{e}_{\text{z}} \tag{2}$$

$$\frac{\partial \theta}{\partial t} = \nabla \cdot (\gamma_{\text{T}} \nabla \theta) + q \tag{3}$$

where $\boldsymbol{u}$, p, θ, ρ, $\boldsymbol{\tau}$, and $g = 9.81$ m/s, represent the mean velocity, pressure, potential temperature, density, stress tensor, and the gravitational constant, respectively. Finally, $\mathbf{e}_{\text{z}}$ is the unit vector in the vertically upward direction. In the momentum equation, $\boldsymbol{f}$ is the source term associated with the Coriolis force. For the energy equation, q represents any external heating source. The hydrostatic and non-hydrostatic parts of the total pressure, potential temperature, and density are denoted by the subscript s and d, respectively. The turbulent thermal diffusivity, γ_{T}, is calculated from the turbulent Prandtl number $\sigma_{\text{T}} = \nu_{\text{T}}/\gamma_{\text{T}}$. The turbulent Prandtl number is a function of the local gradient Richardson number as illustrated below (Leendertse and Liu, 1975; Launder, 1975)

$$R_i = -\frac{g}{\rho_0} \frac{\partial \rho / \partial z}{(\partial u_\tau / \partial z)^2} \tag{4}$$

$$\sigma_{\text{T}} = \sigma_{\text{T}_0} \exp(1.5\, R_i) \tag{5}$$

with u_τ, z, and ρ_0 being the horizontal velocity, the vertical coordinate, and reference density, respectively. For oceanographic flow, the incompressible velocity condition is often used to fulfill the continuity constraint. However, the more general anelastic approximation, where only the time-dependent part is neglected, is considered more appropriate for dynamic meteorology as we are studying herein (Utnes, 2007).

The Boussinesq approximation used in SIMRA consists of modeling density variation based on (Boussinesq, 1897) to take into account the buoyancy forces (Utnes, 2007). The hydrostatic potential temperature used in the momentum equation is calculated using the following state equation

$$\rho_{\text{s}} = \frac{p_{\text{s}}}{R \theta_{\text{s}}} \left(\frac{p_0}{p_{\text{s}}} \right)^{\frac{R}{C_{\text{p}}}} \tag{6}$$

with R being the gas constant and C_{p} the specific heat at constant pressure. The stress tensor is modeled via the Boussinesq hypothesis (Boussinesq, 1877; Schmitt, 2007) which models the turbulent shear stress τ present in the momentum equation as follows

$$\tau_{ij} = \nu_{\text{T}} \left(\frac{\partial u_i}{\partial x_j} + \frac{\partial u_j}{\partial x_i} \right) - \frac{2}{3} k \delta_{ij}. \tag{7}$$

The standard high Reynolds' number $k - \epsilon$ turbulence model with a modification for stratification as shown in Eqs. (8)–(10) is used for the turbulence closure (Launder and Spalding, 1974).

$$\mu_{\text{T}} = C_\mu \frac{\rho k^2}{\epsilon} \tag{8}$$

$$\frac{\mathrm{d}k}{\mathrm{d}t} = \nabla \cdot (\nu_{\mathrm{T}} \nabla k) + P_k + G_\theta - \epsilon \tag{9}$$

$$\frac{\mathrm{d}\epsilon}{\mathrm{d}t} = \nabla \cdot \left(\frac{\nu_{\mathrm{T}}}{\sigma_\epsilon} \nabla \epsilon \right) + (C_1 P_k + C_3 G_\theta) \frac{\epsilon}{k} - C_2 \frac{\epsilon^2}{k} \tag{10}$$

where the production term is given by

$$P_k = \nu_{\mathrm{T}} \left(\frac{\partial u_i}{\partial x_j} + \frac{\partial u_j}{\partial x_i} \right) \frac{\partial u_i}{\partial x_j} \tag{11}$$

and the buoyancy term is given by

$$G_\theta = -\frac{g}{\theta} \frac{\nu_{\mathrm{T}}}{\sigma_{\mathrm{T}}} \frac{\partial \theta}{\partial z}. \tag{12}$$

where σ_ϵ, $C_1 = 1.45$, $C_2 = 1.90$, $C_3 = 0.8$, and $C_\mu = 0.09$ are model constants (Launder and Spalding, 1974). The set of equations solved numerically for estimating mean flow quantities in a fjord surrounded by highly irregular topography includes the three equations given in Eqs. (1)–(3), with the corresponding energy equation solving for potential temperature variation, as well as the turbulence closure formulated in Eqs. (8)–(10).

2.2. Finite element discretization of the governing equations

An overview of the finite element discretization procedure is presented in this section. The work by Utnes (2007) includes a full discussion of the finite element formulation utilized in SIMRA, but we here offer the primary derivation for clarity.

The starting point is the conservative form of the momentum equation together with the anelastic continuity equation, as shown in Eqs. (13) to (16).

$$\nabla \cdot \boldsymbol{q} = 0 \qquad \text{in } \Omega \tag{13}$$

$$\frac{\partial \boldsymbol{q}}{\partial t} + \nabla \cdot (\boldsymbol{u}\boldsymbol{q}^{\mathrm{T}}) = -(\nabla p' + \rho' g \mathbf{e}_{\mathrm{Z}}) + \nabla \cdot (\mu_{\mathrm{T}} \nabla \boldsymbol{u}) - f \mathbf{e}_{\mathrm{Z}} \times \boldsymbol{q} \qquad \text{in } \Omega \tag{14}$$

$$\boldsymbol{u} = \boldsymbol{g}_{\mathrm{D}} \qquad \text{on } \partial\Omega_{\mathrm{D}} \tag{15}$$

$$\mu_{\mathrm{T}} \frac{\partial \boldsymbol{u}}{\partial n} - p\boldsymbol{n} = \boldsymbol{g}_{\mathrm{N}} \qquad \text{on } \partial\Omega_{\mathrm{N}} \tag{16}$$

where $\boldsymbol{q} = \rho_0 \boldsymbol{u}$ with ρ_0 representing the hydrostatic fluid density, $\boldsymbol{u}$ representing the mean velocity, $\boldsymbol{g}_{\mathrm{D}}$, and $\boldsymbol{g}_{\mathrm{N}}$ the Dirichlet and Neumann boundary conditions, respectively.

We now transform the governing equations (partial differential equations (PDE)) into a variational problem. Let $H^1(\Omega)$ and $L^2(\Omega)$ be the classical infinite dimensional Sobolev functions spaces that the velocity $\boldsymbol{u}$ and the pressure p are assumed to belong to in the variational problem, respectively. To include the boundary conditions we introduce the following spaces:

$$U = \left\{ \boldsymbol{v} \in H^1(\Omega) : \boldsymbol{v} = \boldsymbol{g}_{\mathrm{D}} \text{ on } \partial\Omega_{\mathrm{D}} \right\} \tag{17}$$

$$V = \left\{ \boldsymbol{v} \in H^1(\Omega) : \boldsymbol{v} = 0 \text{ on } \partial\Omega_{\mathrm{D}} \right\} \tag{18}$$

$$Q = \left\{ q \in L^2(\Omega) \right\} \tag{19}$$

The variational formulation is obtained by multiplying the momentum and continuity equation with test functions for velocity ($\delta\boldsymbol{u}$) and pressure (δp), respectively, and integrating by parts. To handle the non-homogeneous Dirichlet conditions we split the trial velocities into two parts

$$\boldsymbol{u} = \boldsymbol{u}_{\mathrm{H}} + \boldsymbol{u}_{\mathrm{D}} \tag{20}$$

where $\boldsymbol{u}_{\mathrm{H}} \in V(\Omega)$ obey the homogeneous Dirichlet boundary conditions and will be treated as the unknown trial functions in the variational problem, whereas $\boldsymbol{u}_{\mathrm{D}} \in U(\Omega)$ is the so-called lifting function that we are free to specify as long as it obeys the non-homogeneous Dirichlet and continuity conditions. The variational problem now reads:

Find $\boldsymbol{u}_{\mathrm{H}} \in V(\Omega)$ and $p \in Q(\Omega)$ such that for all $\delta\boldsymbol{u}_{\mathrm{H}} \in V(\Omega)$ and $\delta p \in Q(\Omega)$ we have that:

$$m(\boldsymbol{u}_{\mathrm{H}}, \delta\boldsymbol{u}_{\mathrm{H}}; \rho_0) + c(\boldsymbol{u}_{\mathrm{H}}, \boldsymbol{u}_{\mathrm{H}}, \delta\boldsymbol{u}_{\mathrm{H}}; \rho_0) + a(\boldsymbol{u}_{\mathrm{H}}, \delta\boldsymbol{u}_{\mathrm{H}}; \mu) + d(p, \delta\boldsymbol{u}_{\mathrm{H}}) = l(\delta\boldsymbol{u}_{\mathrm{H}})$$
$$d^{\mathrm{T}}(\boldsymbol{u}_{\mathrm{H}}, \delta p) = 0 \tag{21}$$

where

$$m(\boldsymbol{u}_{\mathrm{H}}, \delta\boldsymbol{u}_{\mathrm{H}}; \rho_0) = \int_\Omega \rho_0 \dot{\boldsymbol{u}}_{\mathrm{H}} \cdot \delta\boldsymbol{u}_{\mathrm{H}} \, \mathrm{d}\Omega \tag{22}$$

$$c(\boldsymbol{u}_{\mathrm{H}}, \boldsymbol{u}_{\mathrm{H}}, \delta\boldsymbol{u}_{\mathrm{H}}; \rho_0) = \int_\Omega \nabla \cdot (\boldsymbol{u}_{\mathrm{H}} \rho_0 \boldsymbol{u}_{\mathrm{H}}) \, \delta\boldsymbol{u}_{\mathrm{H}} \, \mathrm{d}\Omega \tag{23}$$

$$a(\boldsymbol{u}_{\mathrm{H}}, \delta\boldsymbol{u}_{\mathrm{H}}; \mu) = \int_\Omega \mu \nabla \boldsymbol{u}_{\mathrm{H}} \cdot \nabla \delta\boldsymbol{u}_{\mathrm{H}} \, \mathrm{d}\Omega \tag{24}$$

$$d(p, \delta\boldsymbol{u}_{\mathrm{H}}) = \int_\Omega \nabla p \cdot \delta\boldsymbol{u}_{\mathrm{H}} \, \mathrm{d}\Omega \tag{25}$$

$$d^{\mathrm{T}}(\delta\boldsymbol{u}_{\mathrm{H}}, \delta p) = \int_\Omega (\nabla \cdot \delta\boldsymbol{u}_{\mathrm{H}}) \, \delta p \, \mathrm{d}\Omega \tag{26}$$

where $m(\cdot,\cdot;\cdot)$ is the kinematic part, $c(\cdot,\cdot,\cdot;\cdot)$ is the convective term, $a(\cdot,\cdot;\cdot)$ is the diffusive term, $d(\cdot,\cdot)$ is the gradient pressure term, and the $d^{\mathrm{T}}(\cdot,\cdot)$ is the divergence term. The corresponding loading terms are:

$$\begin{aligned} l(\delta\boldsymbol{u}_{\mathrm{H}}) &= l_{\mathrm{B}}(\delta\boldsymbol{u}_{\mathrm{H}}) + l_{\mathrm{C}}(\delta\boldsymbol{u}_{\mathrm{H}}) + l_{\mathrm{N}}(\delta\boldsymbol{u}_{\mathrm{H}}) + l_{\mathrm{D}}(\delta\boldsymbol{u}_{\mathrm{H}}) \\ &= -\int_\Omega \rho' g \mathbf{e}_{\mathrm{Z}} \cdot \delta\boldsymbol{u}_{\mathrm{H}} \, \mathrm{d}\Omega - \int_\Omega f \mathbf{e}_{\mathrm{Z}} \cdot \delta\boldsymbol{u}_{\mathrm{H}} \, \mathrm{d}\Omega \\ &\quad + \int_{\partial\Omega_{\mathrm{N}}} \boldsymbol{g}_{\mathrm{N}} \, \mathrm{d}\partial\Omega - E_{\mathrm{mca}}(\boldsymbol{u}_{\mathrm{D}}, \delta\boldsymbol{u}_{\mathrm{H}}; \rho_0, \rho_0, \mu) \end{aligned} \tag{27}$$

Here, $l_{\mathrm{B}}(\cdot)$ is the buoyancy term, $l_{\mathrm{C}}(\cdot)$ is the loading due to the Coriolis effect, $l_{\mathrm{N}}(\cdot)$ is the Neumann load, and $l_{\mathrm{D}}(\cdot)$ is the loading due to any inhomogeneous Dirichlet boundary conditions. For convenience we have introduced the form $E_{\mathrm{mca}}(\cdot,\cdot;\cdot,\cdot,\cdot) : H^1(\Omega) \times H^1(\Omega) \longrightarrow \boldsymbol{R}$ that is defined as follows:

$$E_{\mathrm{mca}}(\boldsymbol{u}_{\mathrm{D}}, \delta\boldsymbol{u}_{\mathrm{H}}; \rho_0, \rho_0, \mu) = m(\boldsymbol{u}_{\mathrm{D}}, \delta\boldsymbol{u}_{\mathrm{H}}; \rho_0) + c(\boldsymbol{u}_{\mathrm{D}}, \boldsymbol{u}_{\mathrm{D}}, \delta\boldsymbol{u}_{\mathrm{H}}, \rho_0) + a(\boldsymbol{u}_{\mathrm{D}}, \delta\boldsymbol{u}_{\mathrm{H}}, \mu) \tag{28}$$

We now choose finite-dimensional finite element spaces for the approximate velocity $\boldsymbol{u}_{\mathrm{H}}^h$ and pressure p^h

$$U^h(\Omega^h) = \left\{ \boldsymbol{u} \in U \ : \ \boldsymbol{u}|_{\Omega_e} \text{ is } \textit{trilinear} \text{ on all elements } \Omega_e \in \Omega^h \right\} \tag{29}$$

$$V^h(\Omega^h) = \left\{ \boldsymbol{v} \in V \ : \ \boldsymbol{v}|_{\Omega_e} \text{ is } \textit{trilinear} \text{ on all elements } \Omega_e \in \Omega^h \right\} \tag{30}$$

$$Q^h(\Omega^h) = \left\{ \boldsymbol{v} \in Q \ : \ \boldsymbol{v}|_{\Omega_e} \text{ is } \textit{trilinear} \text{ on all elements } \Omega_e \in \Omega^h \right\} \tag{31}$$

and introduce the corresponding finite element basis functions for the velocity and pressure respectively, i.e.,

$$\boldsymbol{u}_{\mathrm{H}}^h(\boldsymbol{x}) = \sum_{i=1}^{N_u} \phi_i(\boldsymbol{x}) (\boldsymbol{u}_{\mathrm{H}}^h)_i = \boldsymbol{\Phi}^{\mathrm{T}} \boldsymbol{u}_{\mathrm{H}}^h \quad \text{for any } \boldsymbol{u}_{\mathrm{H}}^h(\boldsymbol{x}) \in V^h(\Omega^h) = \text{span} \left\{ \phi_i \right\}_{i=1}^{N_u} \tag{32}$$

$$p^h(\boldsymbol{x}) = \sum_{i=1}^{N_p} \psi_i(\boldsymbol{x}) (\boldsymbol{p}^h)_i = \boldsymbol{\Psi}^{\mathrm{T}} \boldsymbol{p}^h \quad \text{for any } p^h(\boldsymbol{x}) \in Q^h(\Omega^h) = \text{span} \left\{ \psi_i \right\}_{i=1}^{N_p}. \tag{33}$$

Now, let the finite element representation of the density be piecewise constant on each element, i.e., $\rho_0^h \in Q^h(\Omega^h)$ which implies that $\boldsymbol{q}_{\mathrm{H}}^h = \rho_0^h \boldsymbol{u}_{\mathrm{H}}^h \in V^h(\Omega^h)$ and the corresponding variationally consistent test functions are the same for $\boldsymbol{q}_{\mathrm{H}}^h$ as for $\boldsymbol{u}_{\mathrm{H}}^h$.

The finite element problem now reads: Find $\boldsymbol{u}_{\mathrm{H}}^h \in V^h(\Omega^h)$ and $p^h \in Q^h(\Omega^h)$ such that for all $\delta\boldsymbol{u}_{\mathrm{H}}^h \in V^h(\Omega^h)$ and $\delta p^h \in Q^h(\Omega^h)$ we have that:

$$m(\boldsymbol{u}_{\mathrm{H}}^h, \delta\boldsymbol{u}_{\mathrm{H}}^h, \rho_0^h) + c(\boldsymbol{u}_{\mathrm{H}}^h, \boldsymbol{u}_{\mathrm{H}}^h, \delta\boldsymbol{u}_{\mathrm{H}}^h; \rho_0^h) + a(\boldsymbol{u}_{\mathrm{H}}^h, \delta\boldsymbol{u}_{\mathrm{H}}^h; \tilde{\boldsymbol{\mu}}_{\mathrm{T}}) + d(p^h, \delta\boldsymbol{u}_{\mathrm{H}}^h) = l(\delta\boldsymbol{u}_{\mathrm{H}}^h)$$
$$d^{\mathrm{T}}(\boldsymbol{u}_{\mathrm{H}}^h, \delta p^h) = 0 \tag{34}$$

Here, ρ_0^h is the elementwise piecewise constant finite element density, and $\tilde{\boldsymbol{\mu}}_{\mathrm{T}}$ is a constitutive matrix defined by the turbulent viscosity μ_{T} and

the matrix terms from the streamline upwind Petrov–Galerkin (SUPG) stabilization (Utnes, 2007). By insertion of Eqs. (32) and (33) we can derive the following algebraic system of equations:

$$\boldsymbol{M}\,\dot{\boldsymbol{q}}_{\mathrm{H}}^{h} + \boldsymbol{C}(\boldsymbol{u}_{\mathrm{H}}^{h})\boldsymbol{q}_{\mathrm{H}}^{h} + \boldsymbol{A}\boldsymbol{u}_{\mathrm{H}}^{h} + \boldsymbol{D}\,\boldsymbol{p}^{h} = \boldsymbol{b} \tag{35}$$

$$\boldsymbol{D}^{\top}\boldsymbol{q}_{\mathrm{H}}^{h} = \boldsymbol{0} \tag{36}$$

with $\boldsymbol{q}_{\mathrm{H}}^{h}$, $\boldsymbol{u}_{\mathrm{H}}^{h}$, and $\boldsymbol{p}_{\mathrm{H}}^{h}$ the nodal vectors. With $\boldsymbol{\Phi}$ and $\boldsymbol{\Psi}$ representing the basis functions for the velocity and pressure field, respectively, the global matrices are given by

$$\boldsymbol{M} = \int_{\Omega} \boldsymbol{\Phi}\,\boldsymbol{\Phi}^{\top}\,\mathrm{d}\Omega, \tag{37}$$

$$\boldsymbol{C}(\boldsymbol{u}_{\mathrm{H}}^{h}) = \int_{\Omega} \boldsymbol{\Phi}\,\boldsymbol{u}_{\mathrm{H}}^{h}\,\nabla\boldsymbol{\Phi}^{\top}\,\mathrm{d}\Omega, \tag{38}$$

$$\boldsymbol{A} = \int_{\Omega} \nabla\boldsymbol{\Phi}\,(\tilde{\boldsymbol{\mu}}_{\mathrm{T}}\nabla\boldsymbol{\Phi}^{\top})\,\mathrm{d}\Omega, \tag{39}$$

$$\boldsymbol{D} = -\int_{\Omega} \nabla\boldsymbol{\Phi}\,\boldsymbol{\Psi}^{\top}\,\mathrm{d}\Omega, \tag{40}$$

$$\boldsymbol{D}^{\top} = -\int_{\Omega} \boldsymbol{\Psi}\,\nabla\boldsymbol{\Phi}^{\top}\,\mathrm{d}\Omega, \tag{41}$$

and the right hand side ($\boldsymbol{b}$) with terms corresponding to buoyancy ($\boldsymbol{b}_{\mathrm{B}}$), the Coriolis's force ($\boldsymbol{b}_{\mathrm{C}}$), the Neumann boundary condition ($\boldsymbol{b}_{\mathrm{N}}$), and any non-homogeneous Dirichlet conditions ($\boldsymbol{b}_{\mathrm{D}}$)

$$\begin{aligned}\boldsymbol{b} &= \boldsymbol{b}_{\mathrm{B}} + \boldsymbol{b}_{\mathrm{C}} + \boldsymbol{b}_{\mathrm{N}} + \boldsymbol{b}_{\mathrm{D}} \\ &= -\int_{\Omega} \boldsymbol{\Phi}\,(\rho' g\mathbf{e}_{z})\,\mathrm{d}\Omega - \int_{\Omega} \boldsymbol{\Phi}\,(f\rho_{0}(\mathbf{e}_{z}\times\boldsymbol{u}))\,\mathrm{d}\Omega \\ &\quad + \int_{\partial\Omega} \boldsymbol{\Phi}\,\boldsymbol{g}_{\mathrm{N}}\,\mathrm{d}\Omega - \left(\tilde{\boldsymbol{M}}\,\dot{\boldsymbol{q}}_{\mathrm{D}}^{h} + \tilde{\boldsymbol{C}}(\boldsymbol{u}_{\mathrm{D}}^{h})\boldsymbol{q}_{\mathrm{D}}^{h} + \tilde{\boldsymbol{A}}\boldsymbol{u}_{\mathrm{D}}^{h}\right).\end{aligned} \tag{42}$$

Here the matrices $\tilde{\boldsymbol{M}}$, $\tilde{\boldsymbol{C}}$, and $\tilde{\boldsymbol{A}}$ correspond to the finite element space without Dirichlet boundary conditions. We do not form these matrices but compute instead the contributions to the right-hand side $\boldsymbol{b}_{\mathrm{D}}$ locally on each element that has an element surface aligned with the Dirichlet boundary $\partial\Omega_{\mathrm{D}}$.

When solving the momentum equation with equal order finite element basis functions for the velocity and the pressure the LBB condition (Ladyzhenskaya, Babuska, and Brezzi) is not satisfied in general. However, we use a projection method (Utnes, 2007) that introduced sufficient stabilization (Gresho and Sani, 1998) to achieve a robust solution algorithm.

The discretized form of the energy equation (3) for the potential temperature, θ, the turbulence kinetic energy equation (9) for the turbulent kinetic energy (TKE), k, and the turbulent dissipation equation (10) for the turbulence dissipation, ϵ, is given as follows (assuming that there is no source term).

$$\boldsymbol{M}\,\dot{\theta}^{h} + \boldsymbol{C}(\boldsymbol{u}^{h})\,\theta^{h} + \boldsymbol{A}_{\theta}\,\theta^{h} = \boldsymbol{0} \tag{43}$$

$$\boldsymbol{M}\,\dot{k}^{h} + \boldsymbol{C}(\boldsymbol{u}^{h})\,k^{h} + \boldsymbol{A}_{k}\,k^{h} = \boldsymbol{M}\left(\boldsymbol{P}_{k}^{h} + \boldsymbol{G}_{\rho}^{h} - \epsilon^{h}\right) \tag{44}$$

$$\boldsymbol{M}\,\dot{\epsilon}^{h} + \boldsymbol{C}(\boldsymbol{u}^{h})\,\epsilon^{h} + \boldsymbol{A}_{\epsilon}\,\epsilon^{h} = \boldsymbol{M}\left\{\overline{\epsilon^{h}/k^{h}}\right\}\left(C_{1}\boldsymbol{P}_{k}^{h} + C_{3}\boldsymbol{G}_{\rho}^{h} - C_{2}\,\epsilon^{h}\right) \tag{45}$$

where $\boldsymbol{A}_{\theta}, \boldsymbol{A}_{k}, \boldsymbol{A}_{\epsilon}$ are matrices corresponding to diffusion of the form given in Eq. (39) (with appropriate changes of diffusivities). The time discretization of the potential temperature equation (Eq. (43)) is done using the Taylor–Galerkin formulation (Zienkiewicz et al., 2000) with the same finite element basis functions as for the velocity components. Here, (k^{h}, ϵ^{h}) are nodal vectors, whereas the ratio $\left\{\overline{\epsilon^{h}/k^{h}}\right\}$ indicates element averaged values, assumed due to the fact that k^{h} and ϵ^{h} are interpolated by the same basis functions (i.e., the same as for the velocity components), and $(\boldsymbol{P}_{k}, \boldsymbol{G}_{\rho})$ are the nodal value of the source terms. The k–ϵ equations are discretized using a semi-implicit method and solved using the projection method similar to the momentum equation.

2.3. AROME and the nested set-up

The Norwegian Meteorological Institute (MET-Norway) and the Swedish Meteorological and Hydrological Institute (SMHI) operate the AROME-MetCoOp model (Meteorological Cooperation on Operational Numerical Weather Prediction), a version of Météo-France's AROME (Applications of Research to Operations at Mesoscale). The works of Seity et al. (2011) and Müller et al. (2017) provide a detailed description of the physics, mathematical models, and implementation.

ECMWF-IFS sets the lateral and upper boundaries of the AROME-MetCoOp model with a horizontal discretization of 739 × 949 grid points. The vertical domain extends 33 km. A horizontal resolution of more than 3 km in mesoscale models does not resolve deep convection. Contrarily, AROME employs 2.5 km, ensuring that convection is considered. The model solves the non-hydrostatic fully compressible Euler equation, meaning that, the diffusive part of the Navier–Stokes equation is omitted. AROME is also classified as a spectral model using semi-implicit discretization because the prognostic variables have a spectral representation based on a double Fourier decomposition. The vertical discretization, on the other hand, uses a finite difference scheme.

Twelve prognostic variables are used in AROME among which are the potential temperature, pressure, velocities, and turbulent kinetic energy (TKE). Parametrization is carried out for microphysics (Lascaux et al., 2006) and turbulence prognostic TKE equation similar to the k equation given in Eq. (9) with a diagnostic mixing length (Cuxart et al., 2000). The exchange of energy and water between the atmosphere and surfaces is done using SURFEX (Masson et al., 2013). Furthermore, radiation is parametrized using the European Centre for Medium-Range Weather Forecasts (ECMWF) radiation parametrizations. Data assimilation is done in upper-air using a 3DVAR data assimilation system. As for the surface assimilation, the analysis is done via optimal interpolation (OI) in which surface temperature, soil temperature, and moisture fields are updated based on analysis increment (Müller et al., 2017). To reduce the errors and uncertainties associated with the stochastic and chaotic nature of the atmospheric flow, such as the fast development of convective cells or turbulence, an ensemble prediction system is preferred over a deterministic approach whereby the initial conditions are not perturbed (Schwartz et al., 2015).

A one-downscaling set-up is used to couple the AROME-MetCoOp model with SIMRA. The outer domain here is the region covered by AROME-MetCoOp while the inner domain is the Sulafjord region with 10 m surface resolution. The interface between these domains includes a relaxation zone where the data from the outer domain are adjusted before interpolation. The temporal interpolation at time t^{*} between t_{k} and t_{k+1}, corresponding to the initial condition of the inner domain, is obtained as follows

$$\phi(\boldsymbol{X}_{i}, t^{*}) = \frac{t_{k+1} - t^{*}}{t_{k+1} - t_{k}}\phi(\boldsymbol{X}_{i}, t_{k}) + \frac{t^{*} - t_{k}}{t_{k+1} - t_{k}}\phi(\boldsymbol{X}_{i}, t_{k+1}) \tag{46}$$

where $t_{k} \le t^{*} \le t_{k+1}$, $k = 1, \ldots, n-1$. With n being the time steps at which the result is produced in the outer domain of AROME-MetCoOp. As for the boundary conditions, spatial interpolation is done on the SIMRA grid. The spatial interpolant is given by

$$\phi(x, y) = \sum_{k=1}^{N} W_{k}(x, y)\hat{\phi}_{k}(x, y) \tag{47}$$

with $W_{k}(x, y)$ being the weight function and $\hat{\phi}_{k}(x, y)$ the local approximation of $\phi(x, y)$. A detailed description of the methodology with the complete set of equations can be found in Holstad and Lie (2000) and Eidsvik et al. (2004).

2.4. Finite element error indicators

Reliability and efficiency are two major challenges in fluid flow simulations. These two challenges may be addressed by error estimation combined with adaptive refinements. A lot of research has been performed on error estimation and adaptive mesh refinement over the years, see e.g. Ainsworth et al. (1989) for an overview of the different *a posteriori error estimation* and corresponding adaptive mesh refinement techniques for handling the discretization error. The work by Kumar et al. (2017) showed a thorough investigation of different recover-based estimators for Poisson problems. These estimates employ a projection technique in order to recover a post-processed quantity (usually the gradient, but may also be applied to the unknown itself) from the FE solution. The error is then estimated by taking the difference between the recovered solution and the FE solution in a suitable norm. The work by Abdullah (2021) extended the so-called Continuous Global L^2 (CGL2) error estimator originally introduced by Zienkiewicz and Zhu (1987) for elasticity problems, to be applicable for Stokes, Navier–Stokes, and Boussinesq problems. Adaptive refinement based on these CGL2 error estimators has been implemented into IFEM, which is an isogeometric finite element toolbox developed by NTNU and SINTEF.

We have herein made use of the CGL2-concept implemented in IFEM for providing error indicators and mesh refinement for Boussinesq flow simulations using SIMRA.

We seek the improved x, y or z component of the velocity gradient

$$\sigma^*(\boldsymbol{x}) = \sum_{i=1}^{N_u} \phi_i^*(\boldsymbol{x})\sigma_i^* = (\boldsymbol{\Phi}^*)^\top \boldsymbol{\sigma}^* \quad \text{for any } \sigma^*(\boldsymbol{x}) \in V^*(\Omega) = \text{span}\left\{\phi_i^*\right\}_{i=1}^{N_*} \tag{48}$$

where $\boldsymbol{\Phi}^*$ is the matrix corresponding to the functions used in the representation of the velocity field, but without any boundary conditions, and σ_i^* is the value of the recovered component of the gradient in the nodes.

The component of the velocity gradient $\sigma^*(\boldsymbol{x})$ defined by Eq. (48) is obtained by a continuous global L^2-projection (potentially weighted with a scalar parameter α) in order to determine the vector of nodal values $\boldsymbol{\sigma}^*$

$$\Pi(\boldsymbol{\sigma}^*) = \int_\Omega \alpha\,(\sigma^* - \sigma^h)^\top \cdot (\sigma^* - \sigma^h)\,\mathrm{d}\Omega \tag{49}$$

By minimizing Eq. (49) with respect to $\boldsymbol{\sigma}^*$ we achieve the following global equations system

$$\boldsymbol{R}\boldsymbol{\sigma}^* = \boldsymbol{b}^* \tag{50}$$

with

$$\boldsymbol{R} = \int_\Omega \alpha\,(\boldsymbol{\Phi}^*)^\top \boldsymbol{\Phi}^*\,\mathrm{d}\Omega\,, \qquad \boldsymbol{b}^* = \int_\Omega \alpha\,(\boldsymbol{\Phi}^*)^\top \sigma^h\,\mathrm{d}\Omega. \tag{51}$$

The above process is called global L2 projection because σ^* is a field that is obtained by projecting the computed gradient components σ^h onto the same function space (without boundary conditions) as used for the computed velocity component u_i^h. If we let $\alpha = \mu_\mathrm{T}$, $\{\sigma_x^h, \sigma_y^h, \sigma_z^h\}^\top = \{\nabla u_x^h, \nabla u_y^h, \nabla u_z^h\}^\top = \nabla \boldsymbol{u}^h$ and similarly for the recovered velocity gradient let $\{\sigma_x^*, \sigma_y^*, \sigma_z^*\}^\top = \{\nabla u_x^*, \nabla u_y^*, \nabla u_z^*\}^\top = \nabla \boldsymbol{u}^*$, then we define the following error indicator for the computed finite element velocity field $\boldsymbol{u}^h$:

$$\begin{aligned}\eta_u^* = a(\boldsymbol{u}^* - \boldsymbol{u}^h, \boldsymbol{u}^* - \boldsymbol{u}^h; \mu_\mathrm{T}) &= \|\sqrt{\mu_\mathrm{T}}\,(\nabla \boldsymbol{u}^* - \nabla \boldsymbol{u}^h)\|_{L^2} \\ &= \left\{\int_\Omega \mu_\mathrm{T}\left(\nabla \boldsymbol{u}^* - \nabla \boldsymbol{u}^h\right)^2\,\mathrm{d}\Omega\right\}^{1/2}\end{aligned} \tag{52}$$

Notice that the accuracy (reliability) of this proposed error indicator depends on the regularity of the true velocity $\boldsymbol{u}$, the mesh topology, and that $V^*(\Omega)$ is of higher polynomial order and regularity than $V^h(\Omega)$ such that $\nabla u^h \notin V^*(\Omega)$ (Abdullah, 2021).

As the pressure field $p^h \in Q^h$ in SIMRA is piecewise constant on each element we let the recovered pressure field p^* be defined by setting $\alpha = 1.0$ and $\sigma^* = p^*$ in Eq. (48) and follow the same CGL2-procedure as described above. We define the following error indicator for the computed finite element pressure p^*:

$$\eta_p^* = \|p^* - p^h\|_{L^2} = \left\{\int_\Omega \left(p^* - p^h\right)^2\,\mathrm{d}\Omega\right\}^{1/2} \tag{53}$$

There are two basic techniques to reduce the discretization error in the finite element: h-refinement, where the element size is reduced, and p-refinement, where the order of the polynomial trial function is increased. However, herein only the h-refinement is performed as the polynomial order for the FE velocity and pressure is fixed in SIMRA. The adaptive procedure chosen in the present study has been to start with an initial mesh $\mathcal{M}_0$ and solve the problem using SIMRA, then compute a posteriori the error indicators for the computed FE velocity and pressure, η_u^* and η_p^* respectively. This has been done using IFEM. The error indicators for each element have then been visualized as color plots in Paraview. Based on the visual inspection in Paraview we have refined the mesh manually to obtain $\mathcal{M}_1$ with smaller elements in the area with the highest value for the error indicators. IFEM facilitates automatic adaptation based on error indicators, but due to the limitation in SIMRA (i.e. requirement of structured mesh topology), we had to do the mesh refinement manually. For the numerical studies performed herein, we usually have done 1–2 mesh refinement steps.

2.5. Wall boundary treatment

Wall functions are required for the high Reynolds number turbulence model outlined in Section 2.1 to eliminate the necessity for a large number of elements near the ground. Wall functions are derived based on the fact that the flow profiles, when normalized by friction velocity and molecular viscosity, collapse into a single curve. This means that the region between the wall and the logarithmic layer is universal (von Kármán, 1930).

For the turbulence parameters, the detailed description of how k and ϵ are handled in near-wall regions is described in Richards and Hoxey (1993) and Parente et al. (2011). For the sake of completeness, the overview of wall treatment is summarized in the following Cebeci and Bradshaw (1977).

The law of the wall for rough surfaces is given by

$$U^+ = \frac{1}{\kappa}\log(Ey^+) - \Delta B \tag{54}$$

where ΔB is a function of the shape and size of the roughness elements, κ is the von Karman constant, and y^+ is calculated as follows

$$y^+ = \frac{C_\mu^{1/4} k_p^{1/2} y_p}{\nu} \tag{55}$$

where $C_\mu = 0.09$, k_p is the TKE at the first grid cell and y_p is the distance from the wall to the first node.

The modification of the law of the wall based on the equations given above to account for the effect of roughness is given by

$$U^+ = \frac{1}{\kappa}\log(E'y^+) \tag{56}$$

with $E' = E\mathrm{e}^{-\kappa\Delta B}$. The near wall turbulent viscosity is obtained from Eq. (56) and given as follows

$$\nu_\mathrm{eff} = \frac{\nu y^+}{\frac{1}{\kappa}\log(E'y^+)} \tag{57}$$

where ν is the viscosity. For the high Reynolds number turbulence model used in SIMRA Eq. (57) is used for the computation of near-wall turbulence viscosity on the conditions that $30 < y^+ < 200$. This condition is a measure for reducing the modeling error related to the wall treatment.

The reduction of modeling error is performed by checking the limit of y_+ values in the post-processing phase. For values outside the range of $30 < y^+ < 200$ the first grid node is refined until a satisfactory non-dimensional wall distance is obtained. It is important to note that, in complex topography, the satisfaction of the above requirement is not possible everywhere in the computational domain.

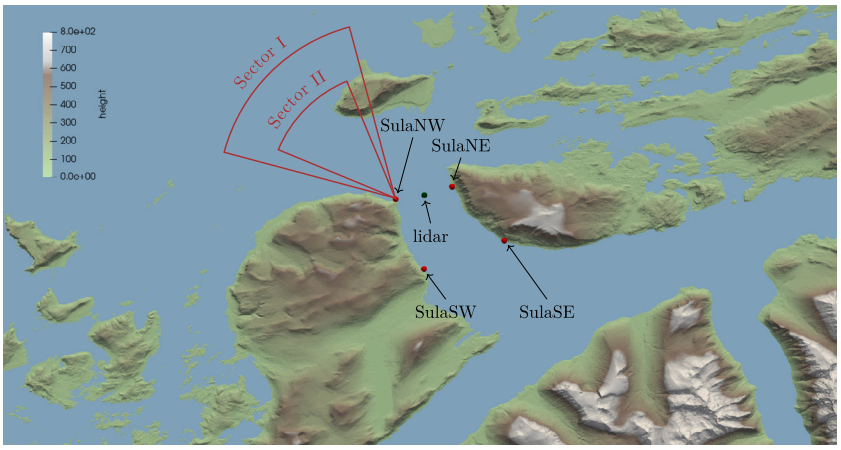

Fig. 1. Digital terrain models with a horizontal resolution of 10 m illustrating the location of the measurement masts and the surrounding topography for Sulafjorden (Midjiyawa et al., 2021).

Table 1
Overview of the met-masts in Sulafjorden: Mast location, mast heights, mast types, sensor heights, boom orientation, boom lengths, and coordinate positions.
Source: Reproduced from Furevik et al. (2020).

Mast				Sensor	Boom		Coordinates
Location	Name	Mast H.(m)	Type	Heights (m)	Orientation (Deg)	Length (m)	UTM32
Kvitneset	SulaNW	100.5	Lattice	92.5, 71.5, 44.5	72, 74, 74	6.1	6924741N, 345142E
Trælbodneset	SulaNE	78.0	Lattice	76.8, 48.3, 27.3	289, 290, 290	6.1	6925267N, 348347E
Langeneset	SulaSW	97.0	Lattice	94.8, 75.0, 50.0, 27.0	81, 81, 81, 81	4.4	6920740N, 346520E
Kårsteinen	SulaSE	63.0	Lattice	62.8, 40.0, 13.4	223, 223, 223	3.6	6922074N, 351140E

3. Observation setup and data processing

Four met-masts have been installed in Sulafjorden, locations hereafter referred to as SulaNW, SulaNE, SulaSW, and SulaSE. These masts are placed in Sulafjorden's north-west, north-east, south-west, and south-east, respectively (Fig. 1). Additionally, the simulation and lidar observation are compared using data that was acquired at a height of around 70 m above the water's surface in the middle of the SulaNW/SulaNE transect. With the exception of employing two lidars, one on either side of the fjord, the setup utilized for lidar measurements is similar to that described in Cheynet et al. (2018). By having two lidars in the same horizontal plane we get two components of the wind velocity being the horizontal components, such that the angle of attack is not provided by the lidar measurements in the work herein. For a complete description of the measurement setup, please see Furevik et al. (2020) and Midjiyawa et al. (2021). Each mast is equipped with three to four anemometers, resulting in a total of 13 anemometers collecting data over several years. Due to the high occurrence of wind speed relevant for buffeting response in November 2020, it is chosen for analysis in this study. The details of the met-masts utilized in Sulafjorden are summarized in Table 1.

For the computation of mean quantities from observation, the decimated 10 Hz data organized in one-hour segments is used directly. These values are compared to numerical simulations based on inlet boundary conditions derived from numerical weather forecast predictions.

Solely one sector was chosen as shown in Fig. 2 (exact dates reported in Tables A.6 and A.7 in Appendix A) to focus only on wind relevant for bridge design, e.g. neutral condition with reasonably high wind speed ($\geq$ 12 m s^{-1}). A total of 47 1-h data series were selected in the northwest, also known as Sector I and identified by the wind direction between 285° and 345°. Only 22 cases are assigned to Sector II once Sector I is further narrowed to the range of 292.5° to 337.5°. This is done in order to investigate the correlation's impact on long upstream fetch.

4. Simulation set-up and analysis

4.1. Computation mesh

The meshes used herein are illustrated in Fig. 3 where $\mathcal{M}_0$ is the initial mesh with a horizontal resolution of typically 150 m, whereas $\mathcal{M}_1$ is a finer mesh that has been optimized for the wind direction of interest using the a-posteriori error indicators described in Section 2.4. A description of the geometric distribution of the elements in the vertical direction is given in Appendix C.

4.2. Basis for analysis

Weather forecasting results from AROME are obtained for every hour. The results are archived and used as the initial conditions for SIMRA simulation and hereby called AROME-SIMRA nested set-up for a macro–micro scale CFD simulations. Only wind speeds above 12 m s^{-1} at SulaNW mast location are used. This guarantees a comparison based on north-western inlet conditions characterized by higher wind speed. However, at SulaNE, SulaSE, and SulaSW, there is a considerable occurrence of wind speed below 12 m s^{-1}. This is due to the fact that the flow field in the vicinity of a fjord, will be strongly affected by topographic effects such as flow channeling (Jackson et al., 1994) due to steep mountain slopes and the resulting flow characterized by adverse pressure gradient leading to acceleration and deceleration of the wind (Mattuella et al., 2015). We first process the measured data which was sampled at a frequency of 10 Hz by an average around every hour (resulting in data points with 60 min spacing). The resulting data is sampled in between such that the data for 11:00 collects averaged data from the interval 10:30–11:30. This data set is then used in comparison with the numerical simulations. Even though the wind speeds are here averaged, we will refer to this as only "wind speeds" (instead of "mean wind speeds") for convenience. This will then be compared to numerical simulations that will be sampled every hour for validation.

Pearson's correlation coefficient (Pearson, 1895) is used to compare observations and numerical simulation (both for the mesoscale and the

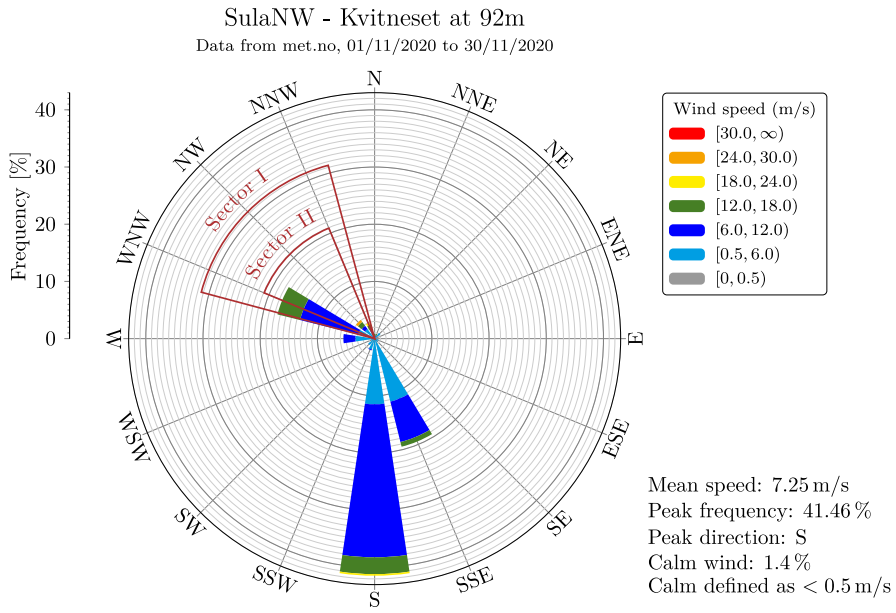

Fig. 2. A wind rose at SulaNW for the month of November 2020. The two sectors with wind speed greater than 12 m s^{-1} used are highlighted with the aim of focusing only on larger wind speeds (mainly coming from NW).

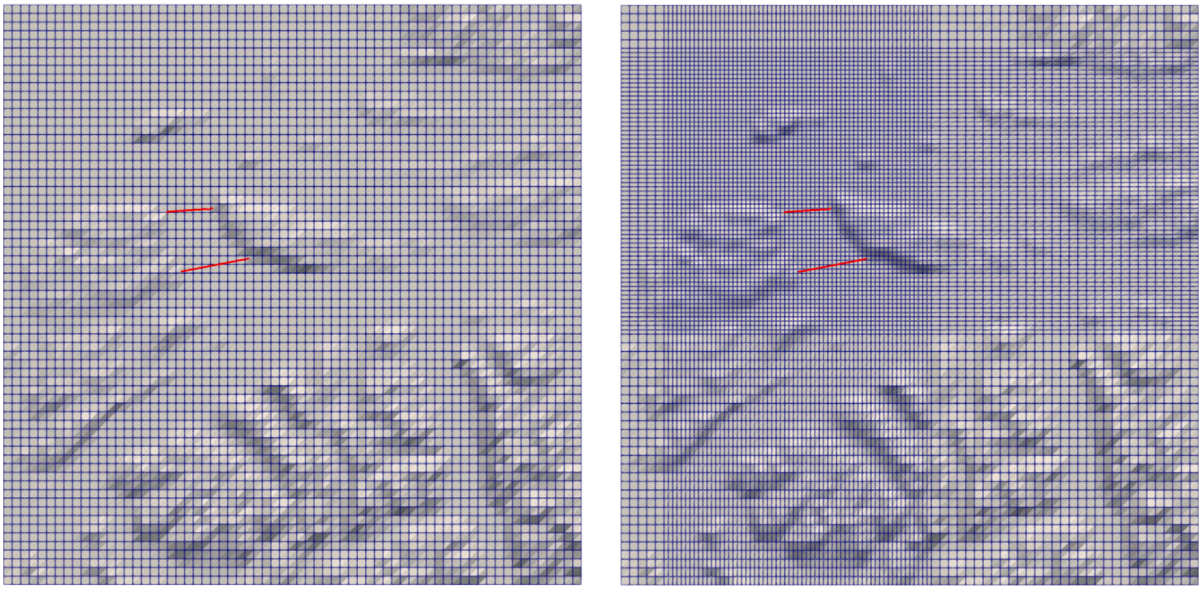

(a) Mesh $\mathcal{M}_0$ with n_{el} = 3 564 450

(b) Mesh $\mathcal{M}_1$ with n_{el} = 7 919 400

Fig. 3. Visualization of the ground surface mesh for the simulations performed herein where the two bridge locations are marked by red lines. Mesh $\mathcal{M}_0$ and $\mathcal{M}_1$ has a minimal horizontal resolution of roughly 150 m and 75 m, respectively. Both meshes use 50 elements in the horizontal direction.

nested meso-microscale). The findings are analyzed by determining the correlation coefficient based on the scatter plots generated between the observation and numerical simulation. For the purpose of completeness, a correlation coefficient of 1 shows a positive relationship between observation and numerical simulation. A coefficient estimated to be −1 indicates a high negative agreement. Lastly, a correlation value of 0 indicates that there is no link between the observations and numerical simulations.

5. Results and discussions

5.1. A-posteriori error analysis

Fig. 4 shows the global L2-projection elemental error indicators η_u^* and η_u^* for velocity and pressure, respectively. We only show the results obtained for the case of 2020-11-19 +06 because it is representative of the results obtained for all hours examined. The notation 2020-11-19 +06 refers to the initial condition from AROME forecasting used in SIMRA which here is November 19th 2020 at 06:00.

The global L2 projection error η_u^* and η_p^* are not uniform in the computational domain, as can be seen. As the element size decreases, the errors computed show a noticeable difference. The error in mesh $\mathcal{M}_0$ is concentrated specifically in the areas of adverse pressure gradient on the west side of the fjord as well as the stagnation point on the east side of Sulafjorden. The refined grid $\mathcal{M}_1$, on the other hand, is distinguished by smaller element sizes in the flow direction as well as regions susceptible to flow re-circulation, separation, and stagnation. The semi-local refinement demonstrates that one may reduce significantly the error indicators for both velocity and pressure by this manual

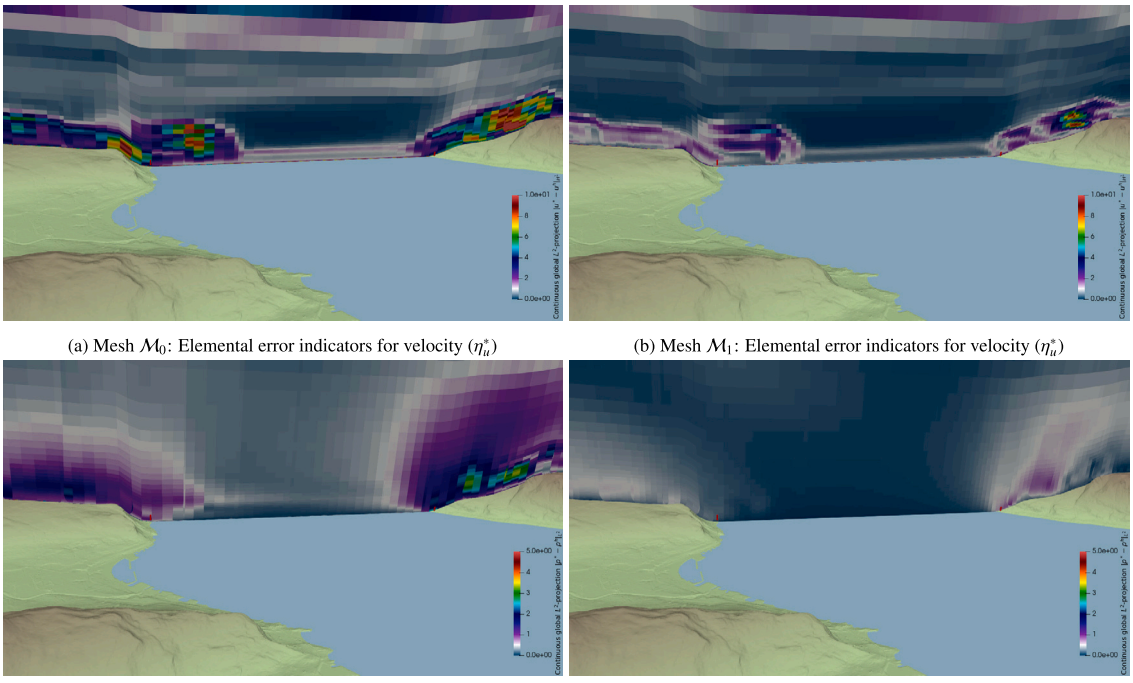

(a) Mesh $\mathcal{M}_0$: Elemental error indicators for velocity (η_u^*)

(b) Mesh $\mathcal{M}_1$: Elemental error indicators for velocity (η_u^*)

(c) Mesh $\mathcal{M}_0$: Elemental error indicators for pressure (η_p^*)

(d) Mesh $\mathcal{M}_1$: Elemental error indicators for pressure (η_p^*)

Fig. 4. *Case 2021-11-19 +06*: The continuous global L2 projection error indicators η_u^* and η_p^* for the mesh $\mathcal{M}_0$ and $\mathcal{M}_1$. The error indicators are shown for a cross-section taken through the masts located at SulaSW and SulaSE. Significant reduction of the error indicators for the refined mesh $\mathcal{M}_1$ is achieved for both the computed FE velocity and FE pressure.

procedure. Therefore, the simulation result presented in the following sections makes use of the grid $\mathcal{M}_1$.

5.2. The overall validation of flow quantities

The comparison of maximum flow quantities and average correlations provide a first-hand disparity or agreement between observations and numerical simulations.

5.2.1. Comparison of maximum flow quantities

Table 2 provides an overview of the comparison of the maximum wind velocity and maximum AoA over all the anemometers. For bridge design, the maximum AoA and wind speed are of interest due to their relevance in bridge structural dynamics. The absolute difference between the observation and AROME-SIMRA for Sector I is $4.88\,\mathrm{m\,s^{-1}}$ and 5.31° for wind speed and AoA, respectively. In Sector II, the differences in wind speed and AoA are $4.88\,\mathrm{m\,s^{-1}}$ and 4.75°, respectively.

The results show no difference between Sector I and II for maximum wind speed. However, a moderate improvement is observed in the prediction of AoA. The AoA is found to be significantly high in general, both for observation and numerical simulation, which is consistent with what was previously observed in Midjiyawa et al. (2021) for all of the observations examined.

The AROME result, used as initial and boundary conditions, is also examined prior to the nested simulations. The results show that, for wind speed, the AROME result is not far-fetched compared to observation and AROME-SIMRA simulations in general. However, for the AoA, significant discrepancies are observed for AROME whereas the results for AROME-SIMRA are significantly better. The vertical wind component, which is crucial for estimating AoA and is more affected by the steep topography near the met-masts than the horizontal components, cannot be accurately predicted by the mesoscale model due to AROME's mesh resolution in the lower part of the surface layer as compared to microscale model's mesh resolution.

5.2.2. Comparison of average correlation coefficient of flow quantities

The average correlation coefficients from Sector I and II are given in Table 3, for both AROME and AROME-SIMRA. As for the AROME results, Sector I gives an overall average correlation coefficient around 0.5 for wind speed and direction. However, 0.25 is obtained for the AoA. Narrowing the sector, improves the AROME results slightly for wind speed only. The AoA, on the other hand, does not improve and for wind direction, the correlation worsens.

The nested setup shows moderate improvement in the average correlation observed for Sector II for wind speed and direction. However, for the AoA, the average correlation, just as in the case of the AROME, has decreased which may be due to the difficulties in modeling vertical winds.

5.3. Correlation between observation and numerical simulation

Tables 4 and 5 show the correlation, for all anemometers, estimated for AROME vs. Observation and AROME-SIMRA vs. observation for Sector I and Sector II, respectively. Figs. 5, 7, and 8 displays the AROME-SIMRA vs. observation scatter plots for the selected mast's wind speed, wind velocity, and AoA at a height of roughly 50 m above the ground. This elevation is chosen as a representative example of the height at which bridges are constructed. The scatter plots for the other elevation analyzed are presented in Appendix B.

The correlation coefficients are all greater than 0.7 for wind speeds. At SulaSW, where there is a high occurrence of low wind speed, the correlations for all four anemometers are approximately 0.9. At SulaNW, SulaNE, and SulaSE, the results show a reasonably good agreement between observation and numerical simulation for wind directions. At SulaSW, where AROME results show a negative correlation, AROME-SIMRA has a considerable increase as well as a positive correlation. As an illustration at SulaSW, a correlation from −0.86 to 0.4 is obtained at the lowest anemometer located at 27 m above ground. The findings highlight the AROME-SIMRA's improvement in modeling wind direction at recirculation zones.

Table 2
Overview of the comparison between observation and numerical model for the two wind sectors selected for all the met-masts in Sulafjorden.

	Sector I			Sector II		
	Obs.	AROME-SIMRA	AROME	Obs.	AROME-SIMRA	AROME
Max. wind speed	28.12	23.24	23.27	28.12	23.24	23.27
Max. AoA	28.28	22.97	3.33	18.37	13.62	3.09

Table 3
Overview of the average correlation coefficient between observation and numerical model for all the met-masts in Sulafjorden.

	Sector I		Sector II	
	AROME-SIMRA	AROME	AROME-SIMRA	AROME
Mean correlation coefficient for wind speed	0.79	0.48	0.83	0.76
Mean correlation coefficient for wind direction	0.76	0.51	0.89	0.37
Mean correlation coefficient for AoA	0.66	0.25	0.60	0.20

Table 4
Table of the correlation coefficient for the comparison AROME vs. Observations and AROME-SIMRA vs. Observations. Wind velocity above $12\,\mathrm{m\,s^{-1}}$ for all elevations (Wind Sector I). The scatter plots corresponding to these results are found in Figs. 5, 7 and 8 and Appendix B. (A-SIMRA is the abbreviation of AROME-SIMRA).

Mast	Anem. height (m)	Wind speed		Wind Dir.		AoA	
		AROME	A-SIMRA	AROME	A-SIMRA	AROME	A-SIMRA
SulaNW	92	0.62	0.76	0.95	0.94	0.59	0.76
	71	0.59	0.74	0.94	0.93	0.62	0.58
	44	0.48	0.71	0.94	0.91	0.74	0.76
SulaNE	76	0.47	0.77	0.95	0.97	0.55	0.74
	48	0.38	0.81	0.94	0.97	0.34	0.82
	27	0.32	0.83	0.93	0.96	0.08	0.89
SulaSW	94	0.59	0.90	0.08	0.52	−0.16	0.71
	75	0.51	0.91	−0.27	0.28	−0.38	0.48
	50	0.44	0.90	−0.67	0.26	−0.65	0.17
	27	0.42	0.89	−0.86	0.40	−0.66	0.20
SulaSE	62	0.39	0.70	0.84	0.94	0.83	0.89
	40	0.36	0.70	0.81	0.91	0.78	0.87
	13	0.34	0.70	0.65	0.75	0.65	0.78
Lidar	70	0.81	0.73	0.96	0.96	–	–

The simulation fails to capture the flow direction at SulaSW on the southwest of Sulafjorden in contrast to the cases of wind speeds. This could be owing to the difficulty of the CFD tool, which employs a two-equation modified standard $k-\epsilon$ turbulence closure, to appropriately model the flow direction in a region with adverse pressure gradient due to the complex topography (Bautista, 2015; Abdi and Bitsuamlak, 2014). The correlation coefficient at SulaSE, on the other hand, decreases as the anemometer height decreases. At 13 m above ground level, the correlation is the lowest. Validating results near the wall is difficult in general due to the difficulties in using the suitable wall function in complex terrain Blocken et al. (2007). The correlation of 0.75 between observation and AROME-SIMRA at 13 m, on the other hand, indicates a relatively good agreement. The topography at SulaSE is steep which further motivates the grid refinement performed, as illustrated in Fig. 6, in order to help reduce the numerical error. The modeling error, on other hand, is handled using the nested configuration. AROME includes detailed modeling of the heat and momentum exchange between the surface and the atmosphere (Müller et al., 2017), which could be decreasing the error associated with wall modeling in the nested system.

For the AoA, the findings reveal a clear distinction between the anemometers positioned on the west and east sides of Sulafjorden when it comes to estimating the angles of attack. The good agreement between the numerical simulation and observation on the eastern side of Sulafjord may be due to the fact that the long fjord fetch between the west and east shores of Sulafjord facilitates the estimation of the vertical wind speed at the mast located on the east side using the AROME-SIMRA. SulaSW, on the southeast shore of Sulafjorden, has the highest AoA. In the same met-mast, the lowest correlation coefficient is also seen. The determination of the AoA is dependent on the accuracy of estimating the horizontal and vertical wind speeds. In addition, estimating vertical wind in complex topography necessitates a precise prediction of flow recirculation, flow channeling, and other peculiar characteristics associated with flow in complex topography. Furthermore, SulaNW met-mast, which is positioned on the flank of a mountain, will most certainly be susceptible to flow separation for north-western flows.

The use of AROME-SIMRA, as a microscale simulation tool, show an improved correlation coefficient, especially at SulaSW whereby flow recirculation and adverse pressure gradient may be the reason why negative correlation is obtained using the mesoscale flow simulation. This shows that, for cases involving complex topography, microscale models such as SIMRA nested to a mesoscale modeling tool may significantly improve the correlation between observation and numerical simulation.

5.4. Flow characteristics in Sulafjord

The correlation coefficient between lidar measurement and numerical simulations are shown in Fig. 9. The correlations are 0.96 and 0.72 for wind direction and wind speed, respectively. This implies that the nested set-up can be used to assess flow characteristics along the bridge span in a location characterized by measurement sparsity.

The velocity magnitude and AoA for the north-western flow that occurred on 2020-11-19 +06 are illustrated in Fig. 10. The results show a small decrease in velocity magnitude at the inlet boundary on Sulafjorden's north-western side. This could be attributed to the

Table 5
Table of the correlation coefficient for the comparison AROME vs. Observations and AROME-SIMRA vs. Observations. Wind velocity above $12\,\mathrm{m\,s^{-1}}$ for all elevations (Wind Sector II). For the sake of brevity, the scatter plots for Sector II are not included. (A-SIMRA is the abbreviation of AROME-SIMRA).

Mast	Height (m)	Wind Speed		Wind Dir.		AoA	
		AROME	A-SIMRA	AROME	A-SIMRA	AROME	A-SIMRA
SulaNW	92	0.81	0.80	0.92	0.90	0.25	0.30
	71	0.79	0.80	0.92	0.90	0.24	0.21
	44	0.76	0.79	0.90	0.87	0.51	0.47
SulaNE	76	0.79	0.87	0.84	0.91	0.75	0.76
	48	0.77	0.88	0.81	0.91	0.67	0.75
	27	0.76	0.86	0.77	0.92	0.66	0.86
SulaSW	94	0.77	0.83	−0.51	0.90	−0.44	0.40
	75	0.77	0.82	−0.56	0.93	−0.52	0.52
	50	0.77	0.81	−0.59	0.95	−0.56	0.63
	27	0.78	0.81	−0.64	0.95	−0.55	0.54
SulaSE	62	0.69	0.87	0.62	0.87	0.69	0.81
	40	0.69	0.86	0.55	0.86	0.55	0.79
	13	0.71	0.83	0.30	0.69	0.40	0.72
Lidar	70	0.80	0.82	0.92	0.92	–	–

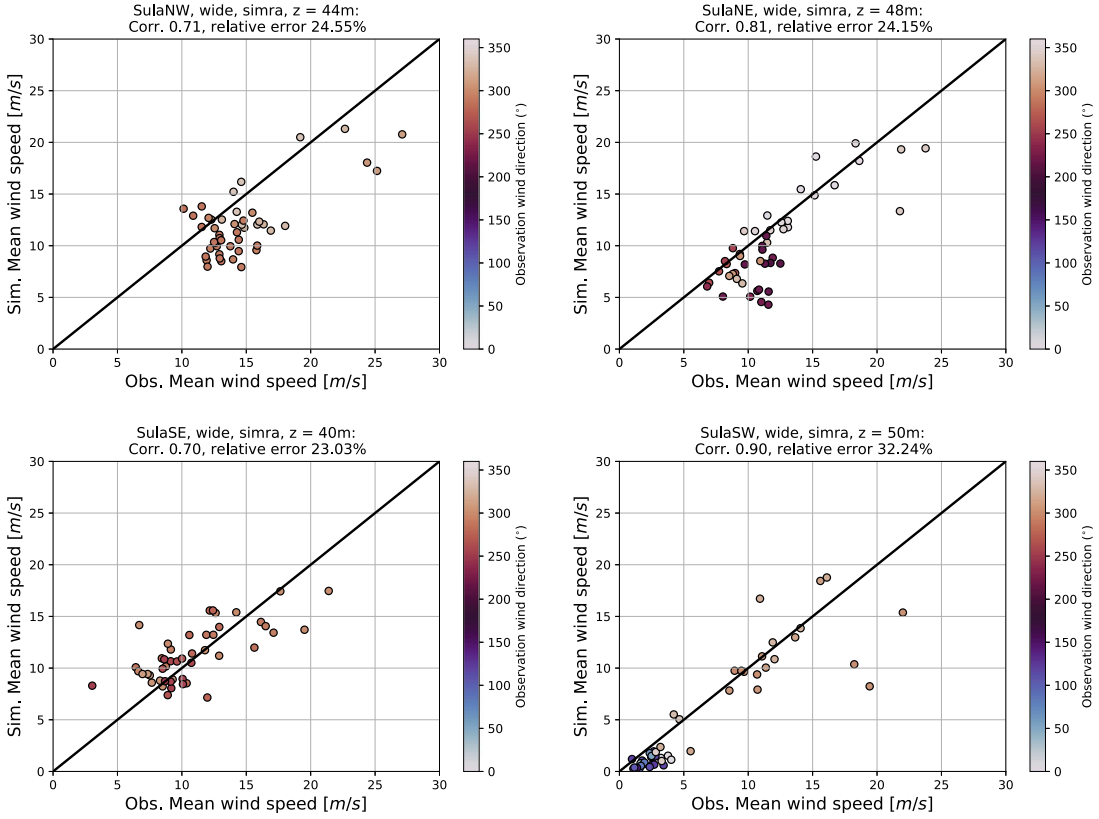

Fig. 5. Estimated correlation between the multiscale AROME-SIMRA against observation for hourly wind speed at Sulafjord, recorded between 01-11-2020 and 30-11-2020 for anemometers located at approximately 50 m above ground (Wind Sector I).

turbulence decay problem associated with the modeling of ABL flows in large domains spanning several kilometers (Blocken et al., 2007). However, after the initial reduction in wind speed near the north-western inlet boundary, the flow is generally undisturbed along the fjord for the direction selected. This implies that the velocity is fairly uniform along the bridge span. Low wind speeds, on the other hand, are observed on the lee side of the mountains, which is typical of flow recirculation regions. For northern flow, not shown here, the island called Godøya may severely influence the flow in the middle of the fjord. The plot in Fig. 10 depicts the horizontality of the flow along the bridge span, which is characterized by a low AoA.

The comparison of the observation and AROME-SIMRA at SulaSW met-mast revealed significant disparities mainly in wind direction and AoA comparison. The results shown in Fig. 10 reveal that the mast is positioned in an area subjected to low wind speed, which is attributable to the mountain range west and northwest of Sulafjorden. As a result, recirculating flows will be common in SulaSW for north-western flows. This is further demonstrated by the velocity normal to the planned bridge line at SulaSW-SulaSE, which is displayed in Fig. 11.

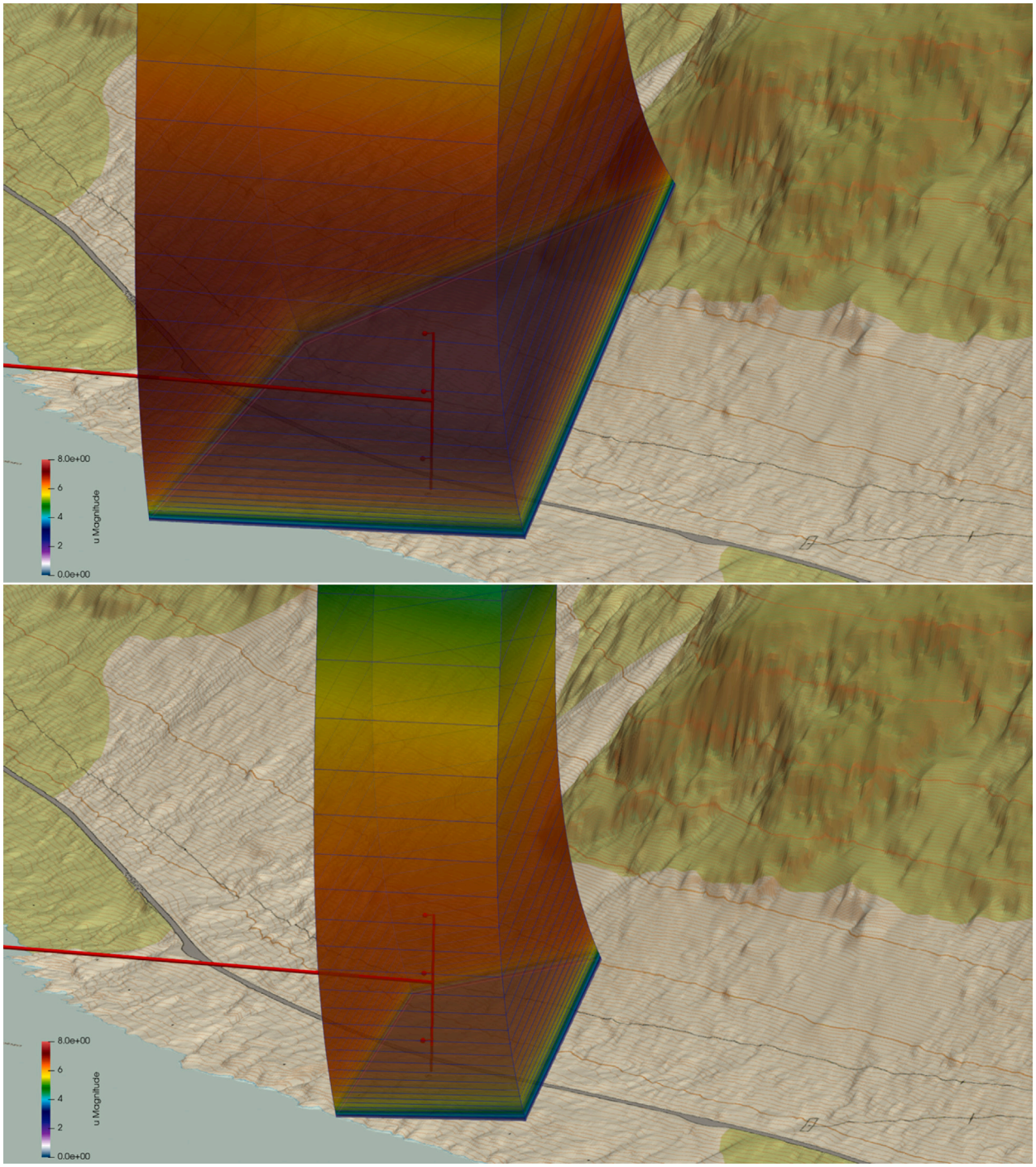

Fig. 6. A single column of elements (at SulaSE) for mesh $\mathcal{M}_0$ (top) and $\mathcal{M}_1$ (bottom), respectively. Due to the steep topography, the first anemometer at SulaSE (13 m above the ground) is not even inside the computational domain for $\mathcal{M}_0$. Which gives even more incentives for grid refinements.

6. Conclusions

The purpose of this research is to assess the potential of using a multiscale numerical tool AROME-SIMRA in the context of bridge design. This is done in order to provide useful design parameters for bridge design in areas where the installation of observation instruments may be prohibitively expensive. To focus on strong wind conditions that are particularly relevant for bridge design, only the north-western flow with wind speeds more than $12\,\mathrm{m\,s^{-1}}$ were chosen at the SulaNW met-mast. The following are the study's main findings:

- The AROME-SIMRA tool is superior to AROME in estimating local wind conditions in terrain-shielded regions. It can estimate mean quantities at sites that may be sheltered by topography or downstream of a mountainous region, making it useful in bridge design. At such challenging sites, the multiscale modeling tool should be used if the resolution is high enough to capture the fine structures

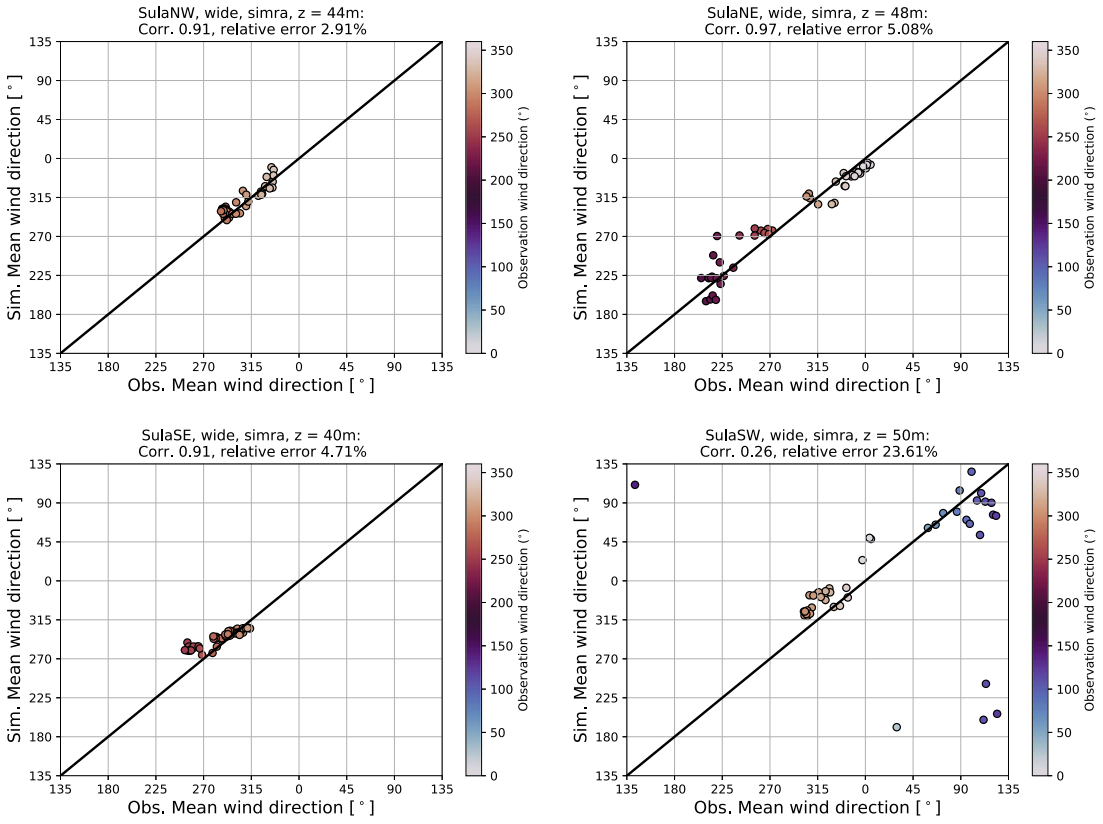

Fig. 7. Estimated correlation between the multiscale AROME-SIMRA against observation for wind direction at Sulafjord, recorded between 01-11-2020 and 30-11-2020 for anemometers located at approximately 50 m above ground (Wind Sector I).

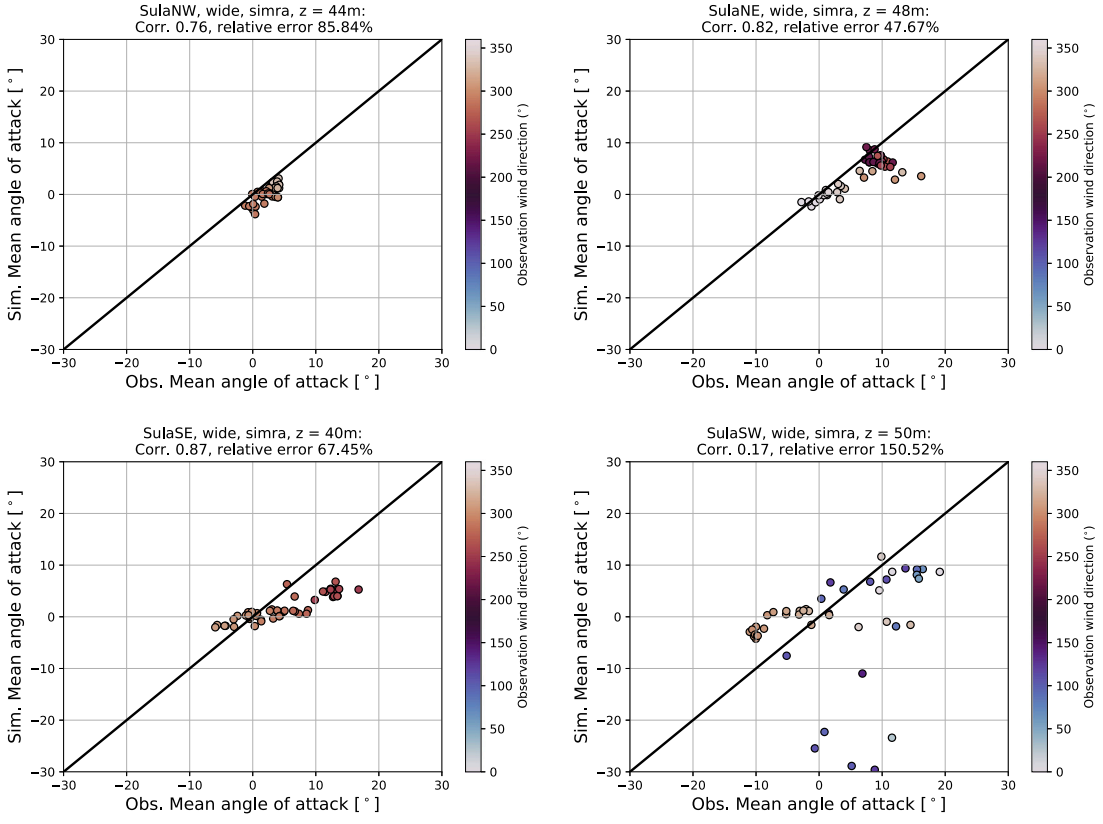

Fig. 8. Estimated correlation between the multiscale AROME-SIMRA against observation for the AoA at Sulafjord, recorded between 01-11-2020 and 30-11-2020 for anemometers located at approximately 50 m above ground (Wind Sector I).

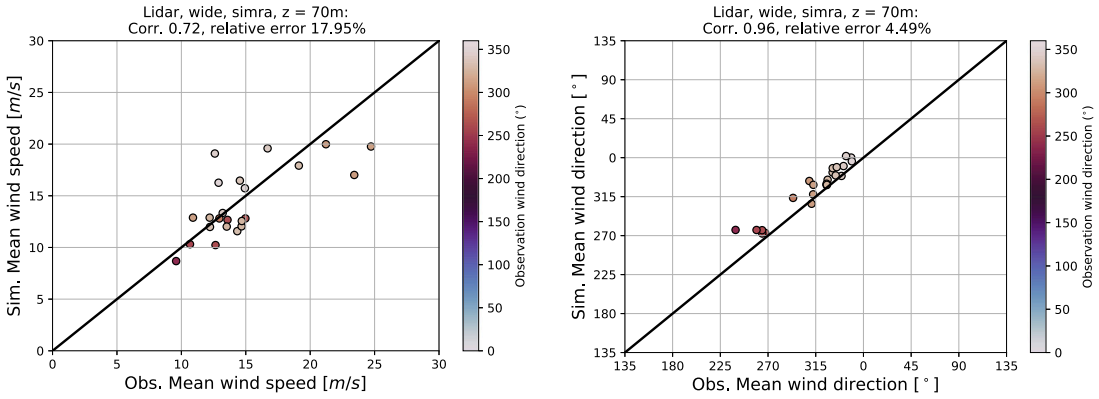

Fig. 9. Estimated correlation between the multiscale AROME-SIMRA against lidar measurements, recorded between 01-11-2020 and 30-11-2020.

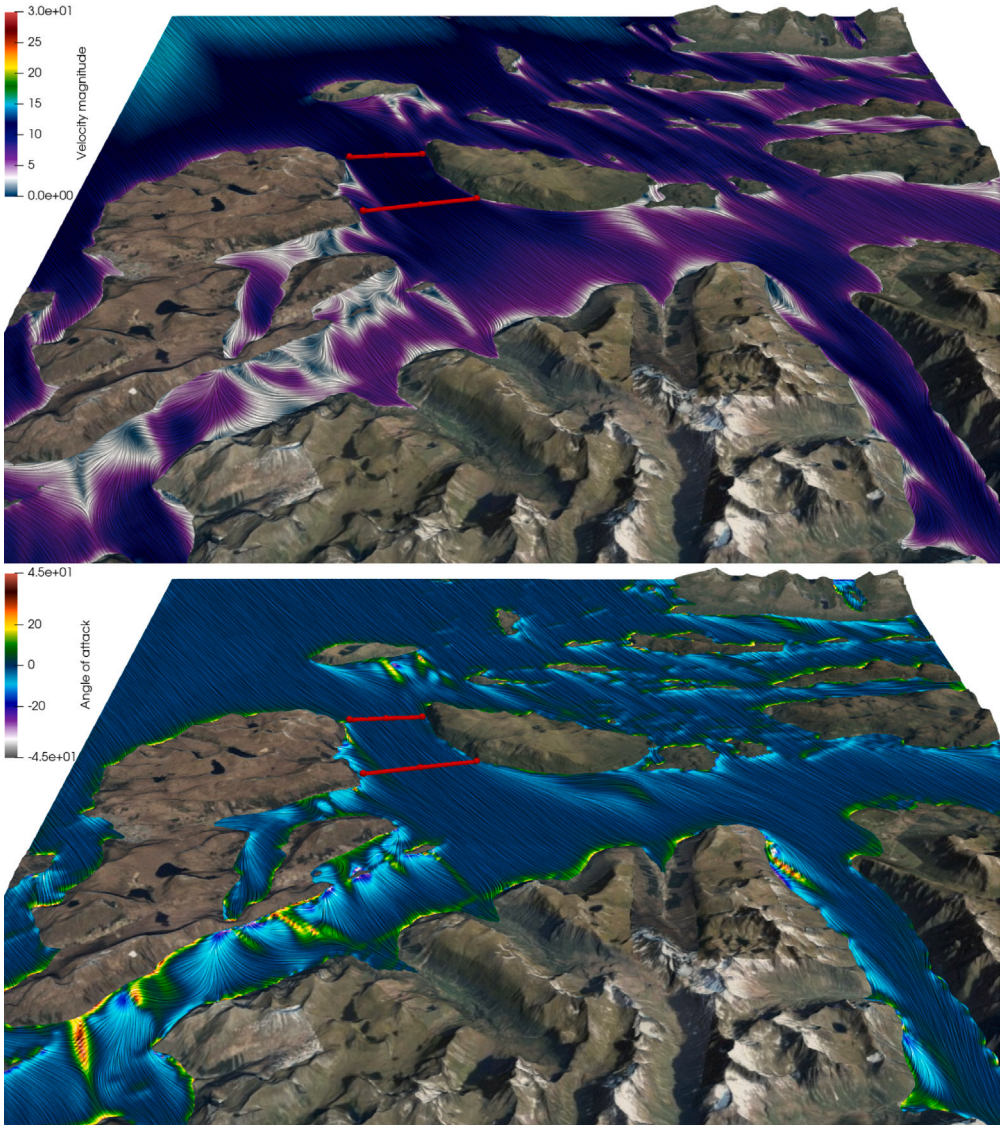

Fig. 10. Bird eye view of velocity magnitude and AoA for the case of the north-western flow on 2020-11-19 +06.

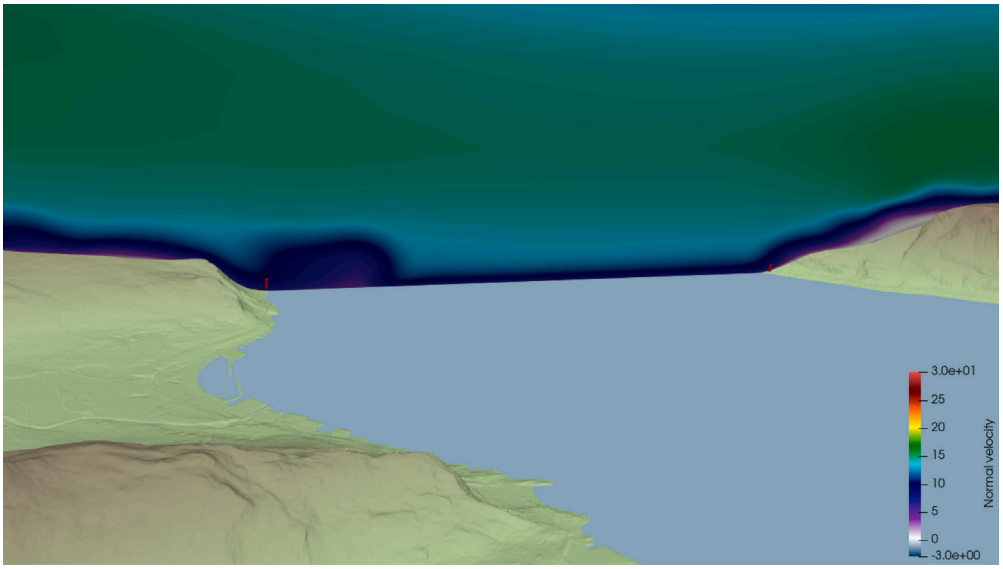

Fig. 11. Normal velocity shown at SulaSW-SulaSE for the case of the north-western flow on 2020-11-19 +06.

Table A.6
Times used in the simulations where the observational data at SulaNW (92 m height) satisfies velocity speeds above 12 m s^{-1} and wind direction within Sector I (total of 47 cases).

Date	Hour
2020-11-05	03:00, 04:00, 05:00, 06:00, 09:00
2020-11-19	04:00, 05:00, 06:00, 0700, 08:00, 09:00, 10:00, 11:00, 12:00
	13:00, 14:00, 16:00, 17:00, 18:00, 19:00, 20:00, 21:00, 22:00
2020-11-21	11:00, 13:00, 14:00, 15:00, 16:00, 17:00, 18:00, 19:00, 20:00, 21:00, 23:00
2020-11-22	00:00, 02:00, 03:00, 04:00, 05:00, 06:00, 07:00, 14:00
	15:00, 16:00, 19:00, 20:00, 21:00

Table A.7
Times used in the simulations (Total of 47 cases) where the observational data at SulaNW (92 m height) satisfies velocity speeds above 12 m s^{-1} and wind direction within Sector II (total of 22 cases).

Date	Hour
2020-11-05	09:00
2020-11-19	04:00, 05:00, 06:00, 0700, 08:00, 09:00, 10:00, 11:00, 12:00
	13:00, 17:00, 18:00, 19:00, 20:00, 21:00, 22:00
2020-11-22	14:00, 15:00, 19:00, 20:00, 21:00

that are prevalent in such locations. In the middle of the fjord, as illustrated by the comparison with lidar measurement, the standalone AROME may be used due to the similarity of the result with the multiscale model for long upstream fetch. However, the nested set-up has the further advantage of using higher resolution in the middle of the fjord which will further improve the accuracy of the result obtained. The numerical simulation, using the nested AROME-SIMRA system, has shown that the flow is mainly horizontal and uniform along the proposed bridge span for the selected wind direction. Therefore, consideration related to the high AoA, and sudden change of wind speed and direction, observed at the mast locations, may be limited only to the design of the bridge towers on the shores of Sulafjorden.

- As mentioned earlier, the AROME-SIMRA couple system consistently showed superior performance compared to the AROME when validated against the real field data collected over a reasonable duration spanning several days. In particular, the findings highlight the AROME-SIMRA's significant improvements of the correlation coefficients of the wind speeds and the wind directions closed to the ground and at recirculation zones. The validated model can now be used with more confidence to make critical decisions pertaining to bridge design at least for the site investigation.
- The a-posteriori error indicators based on continuous global L^2-projection (CGL2) of the error in velocity gradients, $\eta_u^h = \|\sqrt{\mu_T}(\nabla u^* - \nabla u^h)\|_{L^2}$, and pressure $\eta_p^h = \|p^* - p^h\|_{L^2}$, turned out to be useful for semi-local manual mesh optimization. The indicators revealed and quantified that the numerical error associated with the finite element discretization of the momentum, pressure, and potential temperature equation is more concentrated in regions with an adverse pressure gradient.

A new nested system combining AROME-SIMRA and LES (Large Eddy Simulation) may be devised to explore the spectral characteristics

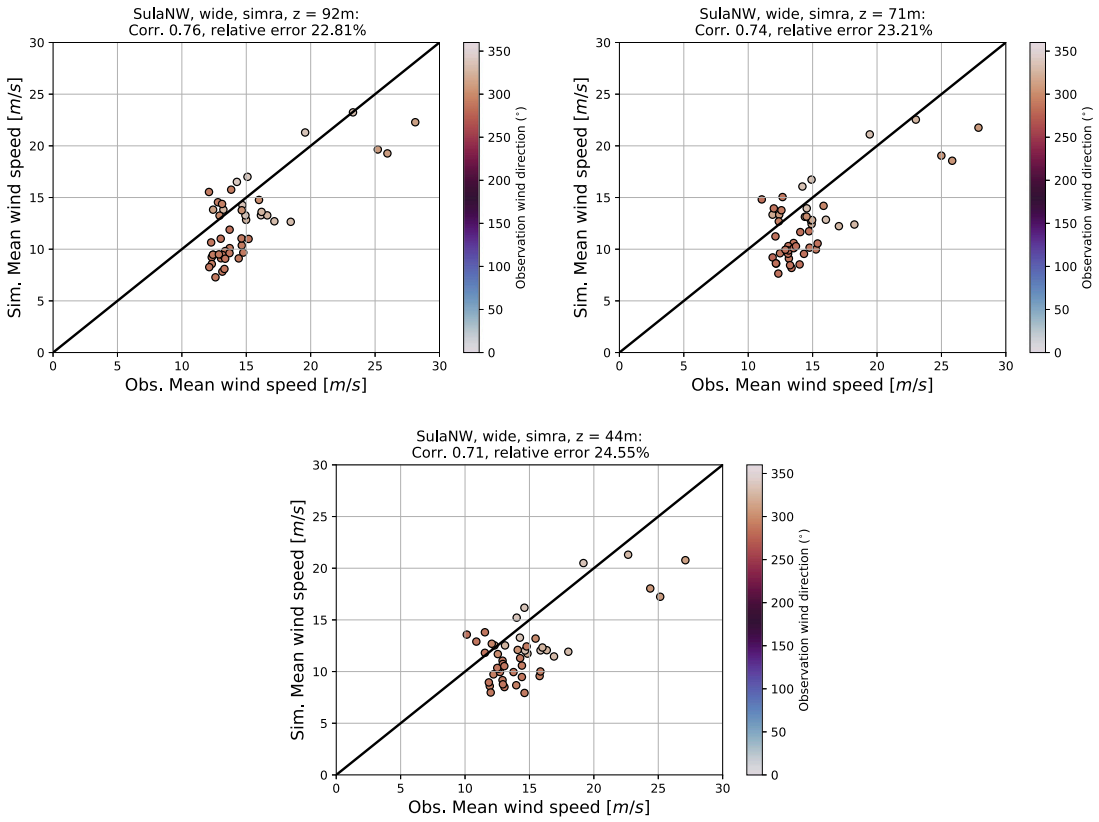

Fig. B.12. Estimated correlation between the multiscale AROME-SIMRA against observation for hourly wind speed at SulaNW, recorded between 01-11-2020 and 30-11-2020.

of turbulence along the proposed bridge span at Sulafjorden. Such numerical simulations may provide a detailed description of the low-frequency part of the turbulence spectra relevant for buffeting response analysis for bridge design (Han et al., 2018).

CRediT authorship contribution statement

Zakari Midjiyawa: Conceptualization, Methodology, Software, Validation, Formal analysis, Investigation, Data curation, Writing – original draft, Writing – review & editing, Visualization. **Jon Vegard Venås:** Methodology, Software, Validation, Formal analysis, Investigation, Data curation, Writing – original draft, Writing – review & editing, Visualization. **Trond Kvamsdal:** Supervision, Project administration, Conceptualization, Methodology, Investigation, Writing – original draft, Writing – review & editing. **Arne Morten Kvarving:** Methodology, Software, Validation, Writing – review & editing, Visualization – review & editing. **Knut Helge Midtbø:** Conceptualization, Methodology, Software, Validation – review & editing. **Adil Rasheed:** Conceptualization, Methodology, Formal analysis, Investigation – review & editing.

Declaration of competing interest

The authors declare that they have no known competing financial interests or personal relationships that could have appeared to influence the work reported in this paper.

Data availability

Data will be made available on request.

Acknowledgments

This work and the measurement campaign are financed by the Norwegian Public Roads Administration as part of the Coastal Highway E39 project in the Mid-Norway. We also want to thank Birgitte R. Furevik and Jørn Kristiansen (Norwegian Meteorological Institute), Joachim Reuder and Etienne Cheynet (Geophysical Institute and Bergen Offshore Wind Centre) for providing the resources and guidance necessary for this work.

Appendix A. Time tables

For reproducibility purposes, we here present an overview of the times at which the data set is extracted.

Appendix B. Scatter plots

For reproducibility purposes, we here present the remaining scatter plots having similar results compared to the scatter plots already shown.

B.1. Wind velocity scatter plots

See Figs. B.12–B.15.

B.2. Wind direction scatter plots

See Figs. B.16–B.18.

B.3. AoA scatter plots

See Figs. B.19–B.21.

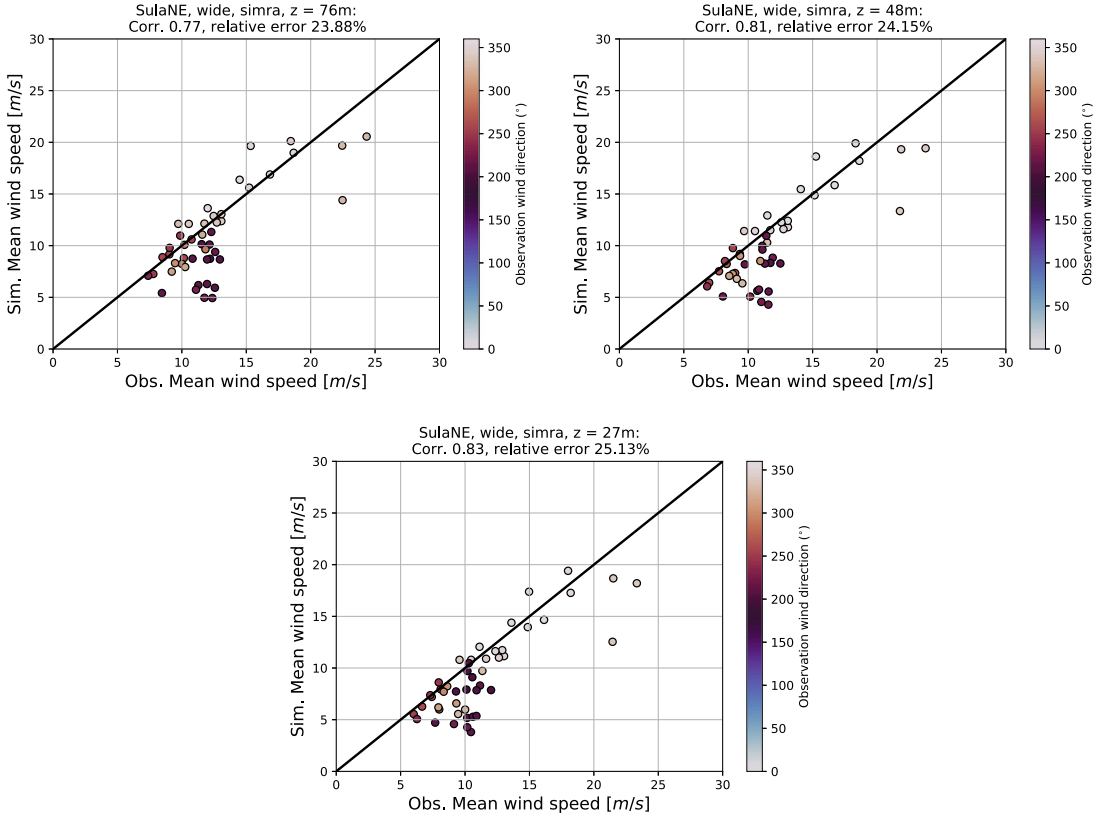

Fig. B.13. Estimated correlation between the multiscale AROME-SIMRA against observation for hourly wind speed at SulaNE, recorded between 01-11-2020 and 30-11-2020.

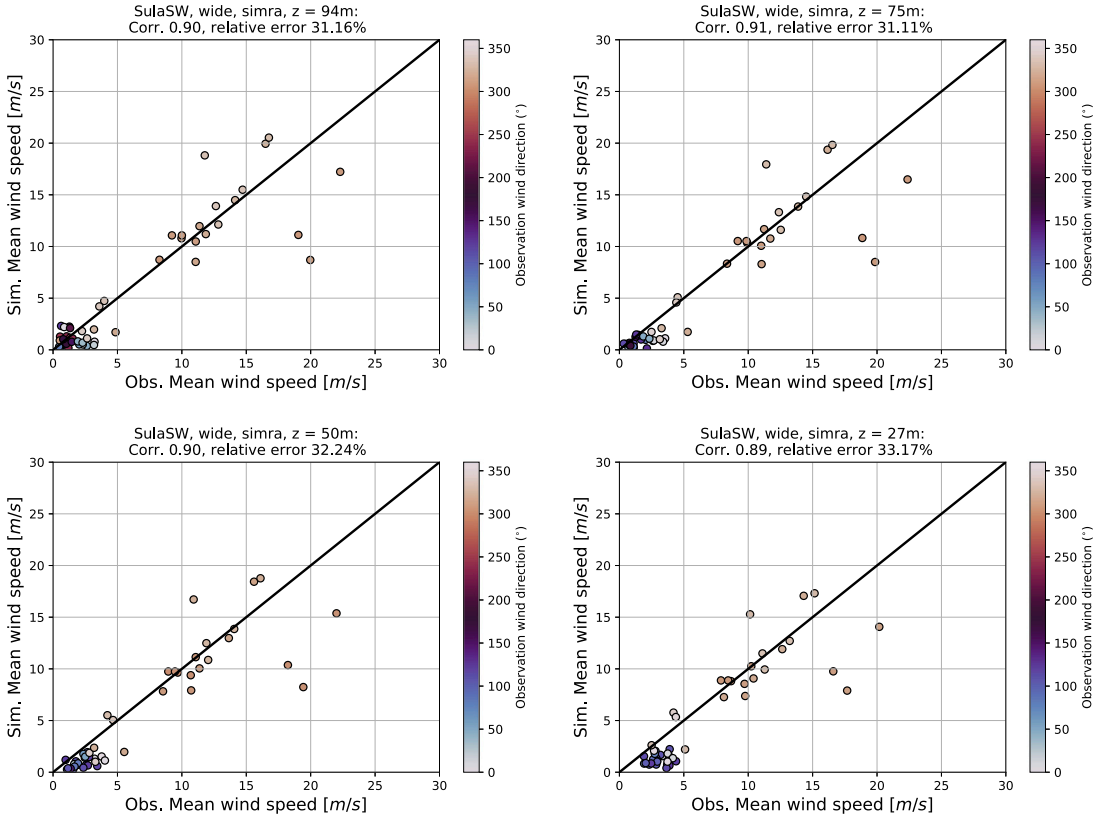

Fig. B.14. Estimated correlation between the multiscale AROME-SIMRA against observation for hourly wind speed at SulaSW, recorded between 01-11-2020 and 30-11-2020.

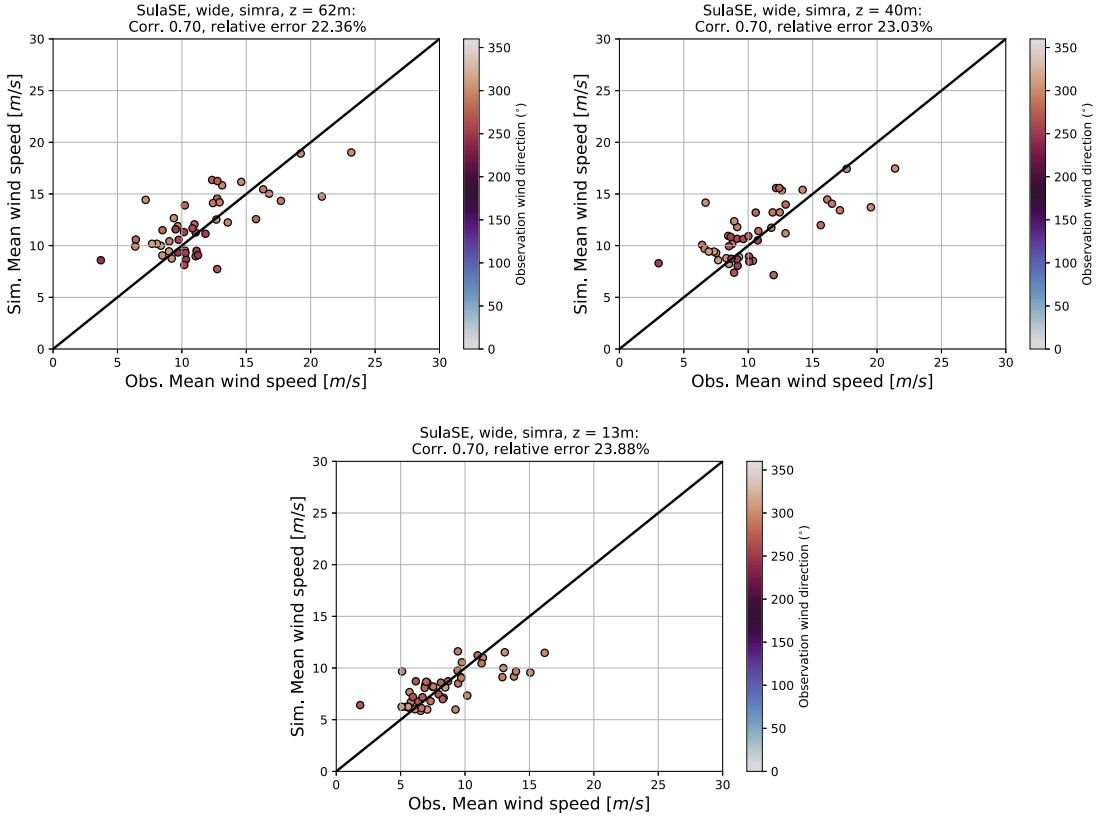

Fig. B.15. Estimated correlation between the multiscale AROME-SIMRA against observation for hourly wind speed at SulaSE, recorded between 01-11-2020 and 30-11-2020.

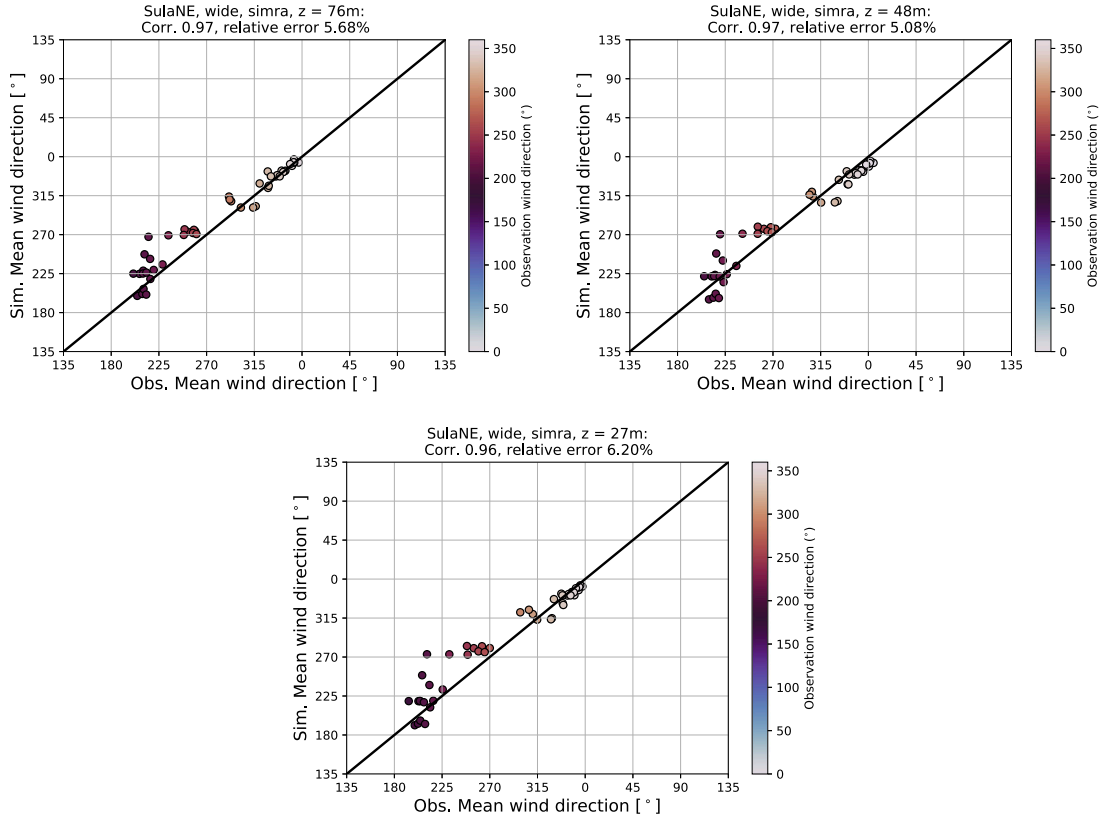

Fig. B.16. Estimated correlation between the multiscale AROME-SIMRA against observation for wind direction at SulaNE, recorded between 01-11-2020 and 30-11-2020.

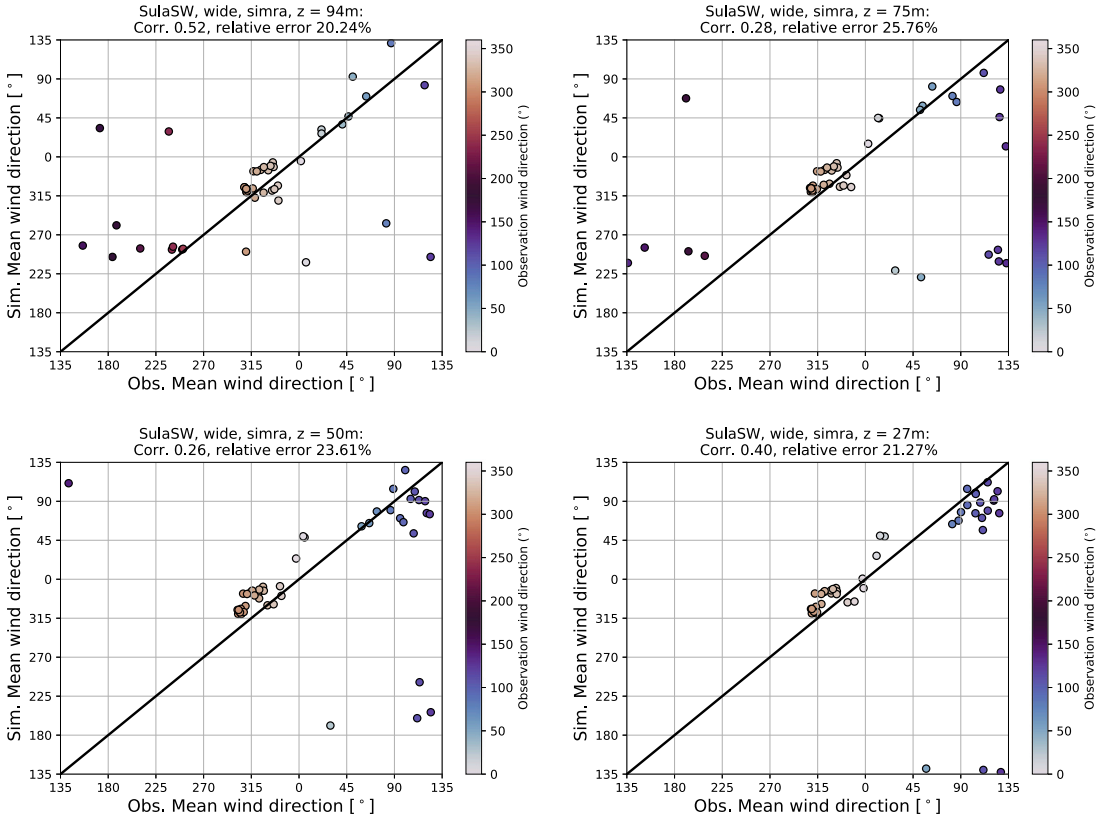

Fig. B.17. Estimated correlation between the multiscale AROME-SIMRA against observation for wind direction at SulaSW, recorded between 01-11-2020 and 30-11-2020.

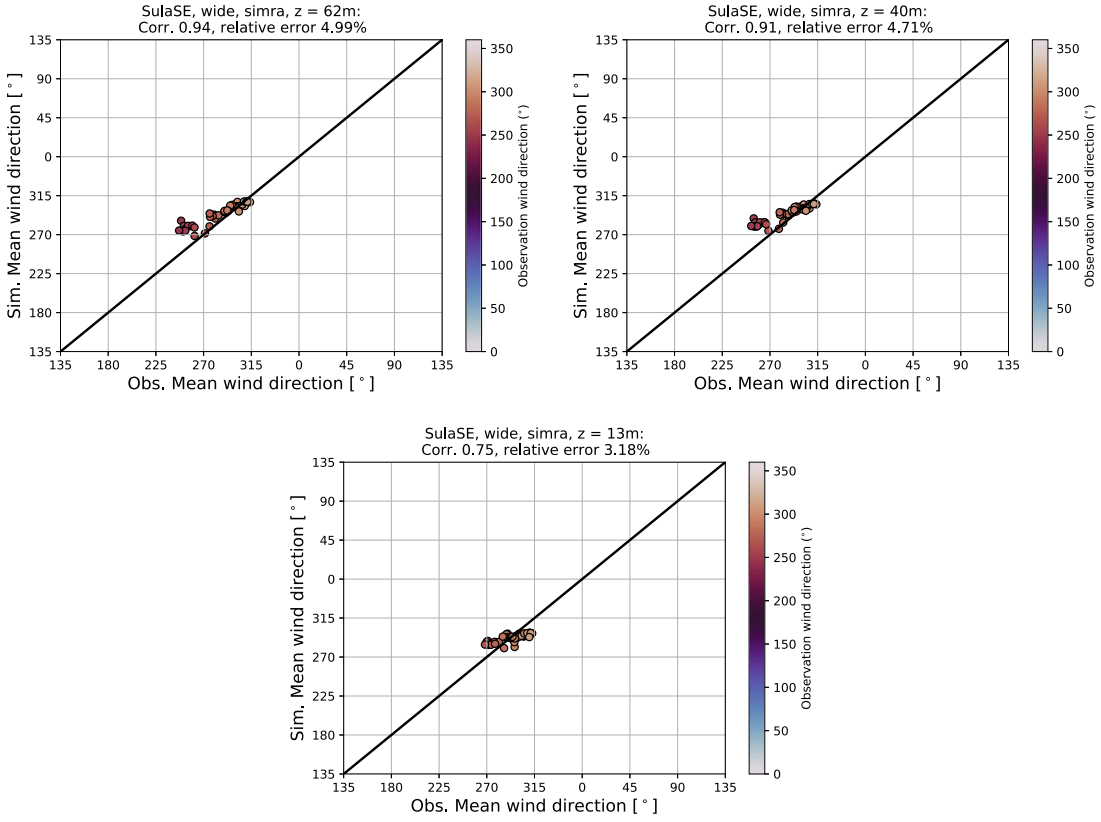

Fig. B.18. Estimated correlation between the multiscale AROME-SIMRA against observation for wind direction at SulaSE, recorded between 01-11-2020 and 30-11-2020.

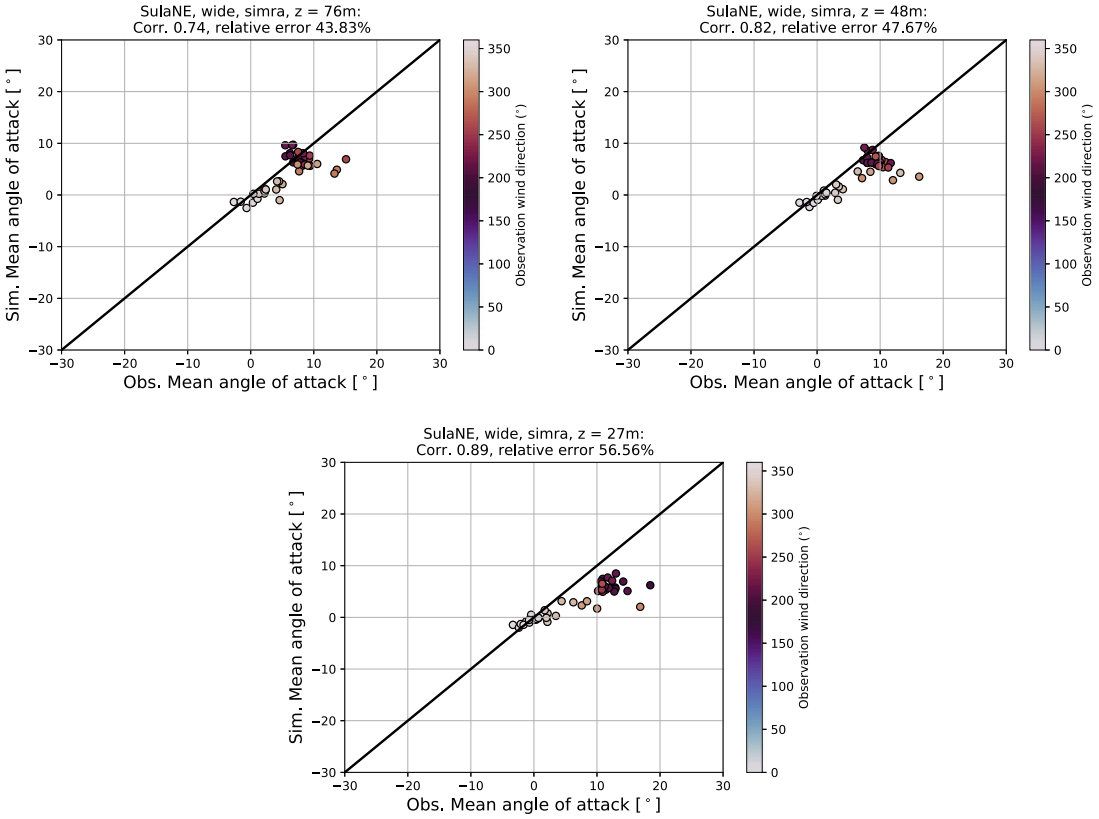

Fig. B.19. Estimated correlation between the multiscale AROME-SIMRA against observation for the angle of attack at SulaNE, recorded between 01-11-2020 and 30-11-2020.

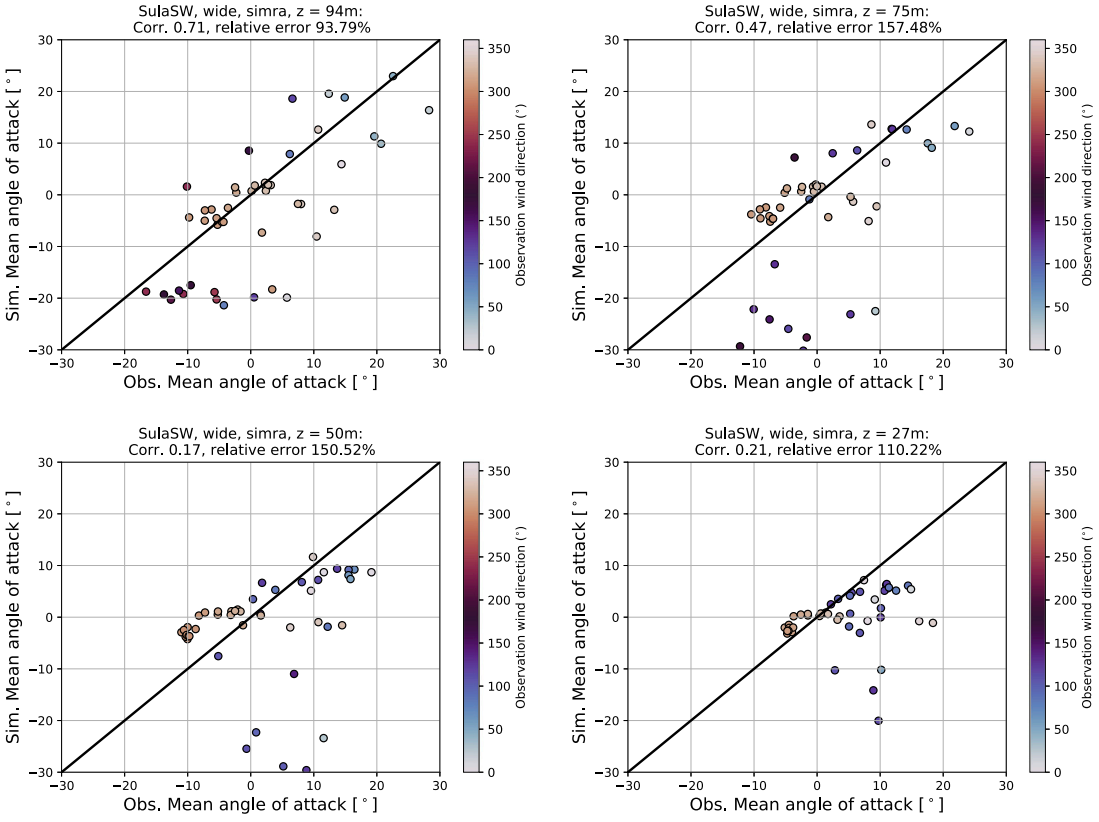

Fig. B.20. Estimated correlation between the multiscale AROME-SIMRA against observation for the angle of attack at SulaSW, recorded between 01-11-2020 and 30-11-2020.

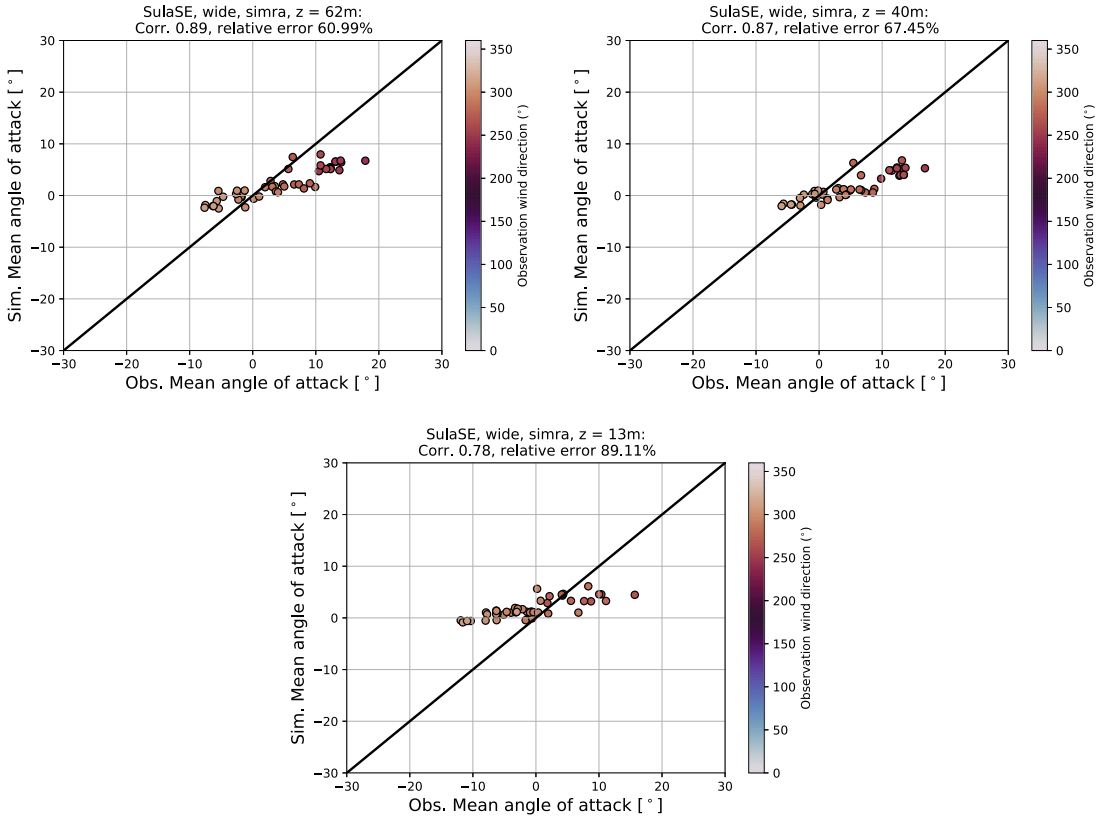

Fig. B.21. Estimated correlation between the multiscale AROME-SIMRA against observation for the angle of attack at SulaSE, recorded between 01-11-2020 and 30-11-2020.

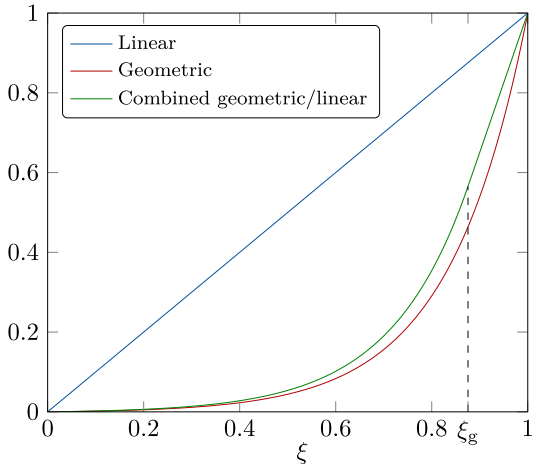

Fig. C.22. Instead of using a simple geometric distribution of the elements in the vertical direction we use a combined geometric and linear distribution.

Appendix C. Geometric distribution

To resolve the logarithmic behavior of the velocity profile near the ground it is important to have a geometric distribution of elements vertically from the ground. This could result in too coarse elements at the upper part of the mesh. To resolve this problem we use a linear distribution of the elements here. To obtain this, we introduce the following distribution (with ξ being a scaled height from the ground to the top of the volumetric mesh)

$$G(\xi) = \begin{cases} b(\alpha^{\xi} - 1) & 0 < \xi \leq \xi_g \\ a(\xi - 1) + 1 & \xi_g < \xi \leq 1 \end{cases} \tag{C.1}$$

where

$$a = b\alpha^{\xi_g} \ln \alpha, \quad b = \frac{1}{\alpha^{\xi_g} - 1 + \alpha^{\xi_g}(1 - \xi_g)\ln \alpha}. \tag{C.2}$$

Here, ξ_g controls the level at which the linear distribution starts and α is the base of the exponential distribution. Note that $G(\xi)$ is smooth at ξ_g. In this work, we choose $\xi_g = 0.875507$ and $\alpha = 468.831657$. The transition to a linear distribution of mesh nodes in the vertical direction is then at $G(\xi_g = 0.875507) = 0.565230$. So with a domain height of $H = 3888.51$ m the linear distribution of elements starts at 2197.9 m for element distributions from sea level. Some distributions are shown in Fig. C.22.

References

Abdi, D.S., Bitsuamlak, G.T., 2014. Wind flow simulations on idealized and real complex terrain using various turbulence models. Adv. Eng. Softw. 75, 30–41.
Abdullah, A., 2021. Adaptive Isogeometric Methods for Boussinesq Problems (PhD dissertation). Department of Mathematical Sciences, Norwegian University of Science and Technology.
Ainsworth, M., Zhu, J., Craig, A., Zienkiewicz, O., 1989. Analysis of the Zienkiewicz–Zhu a-posteriori error estimator in the finite element method. Internat. J. Numer. Methods Engrg. 28 (9), 2161–2174.
Bautista, M.C., 2015. Turbullence Modelling of the Atmospheric Boundary Layer Over Complex Topography (Ph.D. thesis). École de technologie supérieure.
Bechmann, A., 2006. Large-eddy simulation of atmospheric flow over complex terrain.
Bechmann, A., Sørensen, N.N., 2010. Hybrid RANS/LES method for wind flow over complex terrain. Wind Energy: Int. J. Prog. Appl. Wind Power Convers. Technol. 13 (1), 36–50.
Bechmann, A., Sørensen, N.N., 2011. Hybrid RANS/LES applied to complex terrain. Wind Energy 14 (2), 225–237.
Blocken, B., Stathopoulos, T., Carmeliet, J., 2007. CFD simulation of the atmospheric boundary layer: Wall function problems. Atmos. Environ. 41 (2), 238–252.
Boussinesq, J., 1877. Essai sur la thèorie des eaux courantes [Essay on the theory of flowing waters]. Mem. Acad. Sci. 23, 252–260.
Boussinesq, J., 1897. ThÉOrie de L'ÉCoulement Tourbillonnant Et Tumultueux Des Liquides Dans Les Lits Rectilignes a Grande Section, Vol. 1. Gauthier-Villars.

Cao, S., Wang, T., Ge, Y., Tamura, Y., 2012. Numerical study on turbulent boundary layers over two-dimensional hills—effects of surface roughness and slope. J. Wind Eng. Ind. Aerodyn. 104, 342–349.

Castagna, J., Yao, Y., Yao, J., 2012. Numerical simulation of a turbulent flow over an axisymmetric hill. In: 50th AIAA Aerospace Sciences Meeting Including the New Horizons Forum and Aerospace Exposition. p. 98.

Cebeci, T., Bradshaw, P., 1977. Momentum Transfer in Boundary Layers. Washington.

Cheynet, E., Jakobsen, J., Snæbjörnsson, J., Ágústsson, H., Harstveit, K., 2018. Complementary use of wind lidars and land-based met-masts for wind measurements in a wide fjord. In: Journal of Physics: Conference Series no. 1 in 1104. IOP Publishing, 012028.

Cheynet, E., Liu, S., Ong, M.C., Jakobsen, J.B., Snæbjörnsson, J., Gatin, I., 2020. The influence of terrain on the mean wind flow characteristics in a fjord. J. Wind Eng. Ind. Aerodyn. 205, 104331.

Cuxart, J., Bougeault, P., Redelsperger, J.-L., 2000. A turbulence scheme allowing for mesoscale and large-eddy simulations. Q. J. R. Meteorol. Soc. 126 (562), 1–30.

Ding, L., Street, R.L., 2003. Numerical study of the wake structure behind a three-dimensional hill. J. Atmos. Sci. 60 (14), 1678–1690.

Eidsvik, K.J., 2005. A system for wind power estimation in mountainous terrain. prediction of askervein hill data. Wind Energy 8 (2), 237–249.

Eidsvik, K.J., Holstad, A., Lie, I., Utnes, T., 2004. A prediction system for local wind variations in mountainous terrain. Bound.-Lay. Meteorol. 112 (3), 557–586.

Furevik, B.R., Ágústson, H., Lauen Borg, A., Zakari, M., Nyhammer, F., Gausen, M., 2020. Meteorological observations in tall masts for mapping of atmospheric flow in Norwegian fjords. Earth Syst. Sci. Data Discuss. 1–28.

Furevik, B., Ágústsson, H., Borg, A.L., Nyhammer, F., 2019. The E39 Coastal Highway Observational Dataset – Atmospheric Flow in Complex Coastal Terrain in Mid-Norway. Tech. rep, Norwegian Meteorological Institute.

Gresho, P.M., Sani, R.L., 1998. Incompressible Flow and the Finite Element Method. Volume 1: Advection-Diffusion and Isothermal Laminar Flow. John Wiley and Sons, Inc., New York, NY (United States).

Han, Y., Shen, L., Xu, G., Cai, C., Hu, P., Zhang, J., 2018. Multiscale simulation of wind field on a long-span bridge site in mountainous area. J. Wind Eng. Ind. Aerodyn. 177, 260–274.

Hargreaves, D.M., Wright, N.G., 2007. On the use of the k–ϵ model in commercial CFD software to model the neutral atmospheric boundary layer. J. Wind Eng. Ind. Aerodyn. 95 (5), 355–369.

Holstad, A., Lie, I., 2000. A Model System for Prediction of Wind Conditions Around Airports. Tech. Rep. 113, The Norwegian Meteorological Institute.

Jackson, P.L., Steyn, D.G., Jackson, P.L., Steyn, D.G., 1994. Gap winds in a fjord. Part I: Observations and numerical simulation. Mon. Weather Rev. 122, 2645–2665.

Kumar, M., Kvamsdal, T., Johannessen, K.A., 2017. Superconvergent patch recovery and a posteriori error estimation technique in adaptive isogeometric analysis. Comput. Methods Appl. Mech. Engrg. 316, 1086–1156.

Lascaux, F., Richard, E., Pinty, J.-P., 2006. Numerical simulations of three different MAP IOPs and the associated microphysical processes. Q. J. R. Meteorol. Soc. 132 (619), 1907–1926.

Launder, B.E., 1975. On the effects of a gravitational field on the turbulent transport of heat and momentum. J. Fluid Mech. 67 (3), 569–581.

Launder, B., Spalding, D., 1974. The numerical computation of turbulent flows. Comput. Methods Appl. Mech. Engrg. 3 (2), 269–289.

Leendertse, J.J., Liu, D.S.-K., 1975. A Three-Dimensional Model for Estuaries and Coastal Seas: Volume II, Aspects of Computation. Tech. rep, RAND Corporation.

Maronga, B., Gryschka, M., Heinze, R., Hoffmann, F., Kanani-Sühring, F., Keck, M., Ketelsen, K., Letzel, M.O., Sühring, M., Raasch, S., 2015. The Parallelized Large-Eddy Simulation Model (PALM) version 4.0 for atmospheric and oceanic flows: model formulation, recent developments, and future perspectives. Geosci. Model Dev. 8, 2515–2551.

Masson, V., Le Moigne, P., Martin, E., Faroux, S., Alias, A., Alkama, R., Belamari, S., Barbu, A., Boone, A., Bouyssel, F., Brousseau, P., Brun, E., Calvet, J.-C., Carrer, D., Decharme, B., Delire, C., Donier, S., Essaouini, K., Gibelin, A.-L., Giordani, H., Habets, F., Jidane, M., Kerdraon, G., Kourzeneva, E., Lafaysse, M., Lafont, S., Lebeaupin Brossier, C., Lemonsu, A., Mahfouf, J.-F., Marguinaud, P., Mokhtari, M., Morin, S., Pigeon, G., Salgado, R., Seity, Y., Taillefer, F., Tanguy, G., Tulet, P., Vincendon, B., Vionnet, V., Voldoire, A., 2013. The SURFEXv7.2 land and ocean surface platform for coupled or offline simulation of earth surface variables and fluxes. Geosci. Model Dev. 6 (4), 929–960.

Mattuella, J., Loredo-Souza, A., Vecina, T., Petry, A., 2015. Experimental and numerical evaluation of micrositing in complex areas: Speed up effect analysis. In: Conference: 14th International Conference on Wind Engineering - ICWE 14At: Porto Alegre.

Midjiyawa, Z., Cheynet, E., Reuder, J., Ágústsson, H., Kvamsdal, T., 2021. Potential and challenges of wind measurements using met-masts in complex topography for bridge design: Part 1–Integral flow characteristics. J. Wind Eng. Ind. Aerodyn. 104584.

Müller, M., Homleid, M., Ivarsson, K.-I., Køltzow, M.A., Lindskog, M., Midtbø, K.H., Andrae, U., Aspelien, T., Berggren, L., Bjørge, D., et al., 2017. AROME-MetCoOp: A Nordic convective-scale operational weather prediction model. Weather Forecast. 32 (2), 609–627.

Parente, A., Gorlé, C., Van Beeck, J., Benocci, C., 2011. Improved k–ϵ model and wall function formulation for the RANS simulation of ABL flows. J. Wind Eng. Ind. Aerodyn. 99 (4), 267–278.

Pearson, K., 1895. VII. Note on regression and inheritance in the case of two parents. Proc. R. Soc. Lond. 58 (347–352), 240–242.

Rasheed, A., Sørli, K., 2014. A multiscale turbulence prediction and alert system for airports in hilly regions. In: 2014 IEEE Aerospace Conference. pp. 1–10.

Rasheed, A., Sørli, K., Holdahl, R., Kvamsdal, T., 2012. A multiscale approach to micrositing of wind turbines. Energy Procedia 14, 1458–1463.

Richards, P., Hoxey, R., 1993. Appropriate boundary conditions for computational wind engineering models using the k–ϵ turbulence model. J. Wind Eng. Ind. Aerodyn. 46, 145–153.

Scanlan, R., 1978a. The action of flexible bridges under wind, I: flutter theory. J. Sound Vib. 60 (2), 187–199.

Scanlan, R.H., 1978b. The action of flexible bridges under wind, II: Buffeting theory. J. Sound Vib. 60 (2), 201–211.

Schmitt, F.G., 2007. About Boussinesq's turbulent viscosity hypothesis: Historical remarks and a direct evaluation of its validity. Compt. R. Méc. 335 (9), 617–627.

Schwartz, C.S., Romine, G.S., Weisman, M.L., Sobash, R.A., Fossell, K.R., Manning, K.W., Trier, S.B., 2015. A real-time convection-allowing ensemble prediction system initialized by mesoscale ensemble Kalman filter analyses. Weather Forecast. 30 (5), 1158–1181.

Seity, Y., Brousseau, P., Malardel, S., Hello, G., Bénard, P., Bouttier, F., Lac, C., Masson, V., 2011. The AROME-France Convective-Scale Operational Model. Mon. Weather Rev. 139 (3), 976–991.

Simiu, E., Scanlan, R.H., 1996. Wind Effects on Structures: Fundamentals and Applications to Design, third ed. John Wiley New York.

Tabib, M.V., Midtbø, K.H., Skaslien, T., Rasheed, A., Kvamsdal, T., 2020. Towards understanding wind impact for drone operations: A comparison of wind models operating on different scales in a nested multiscale set-up. In: 14th International Conference on CFD in 6 Oil & Gas, Metallurgical and Process Industries SINTEF, Trondheim, Norway, October 12–14, 2020. SINTEF Academic Press, pp. 155–162.

Utnes, T., 2007. Modelling of stratified geophysical flows over variable topography. In: Hasle, G., Lie, K.-A., Quak, E. (Eds.), Geometric Modelling, Numerical Simulation, and Optimization: Applied Mathematics At SINTEF. Springer, Berlin, Heidelberg, pp. 361–390.

Utnes, T., Eidsvik, K., 1996. Turbulent flows over mountainous terrain modelled by the Reynolds equations. Bound.-Lay. Meteorol. 79 (4), 393–416.

von Kármán, T., 1930. Mechanische ahnlichkeit und turbulenz. Math.-Phys. Klasse.

Wu, T., Kareem, A., 2012. An overview of vortex-induced vibration (VIV) of bridge decks. Front. Struct. Civ. Eng. 6 (4), 335–347.

Zienkiewicz, O.C., Taylor, R.L., Taylor, R.L., Taylor, R.L., 2000. The finite element method: solid mechanics, Vol. 2. Butterworth-heinemann.

Zienkiewicz, O.C., Zhu, J.Z., 1987. A simple error estimator and adaptive procedure for practical engineerng analysis. Internat. J. Numer. Methods Engrg. 24 (2), 337–357.